J. Fluid Mech. (2008), *vol.* 613, *pp.* 95–124. © 2008 Cambridge University Press
doi:10.1017/S0022112008003078 Printed in the United Kingdom

Boundary-layer transition at high free-stream disturbance levels – beyond Klebanoff modes

M. E. GOLDSTEIN[1] AND ADRIAN SESCU[2]

[1]National Aeronautics and Space Administration, Glenn Research Center, Cleveland, OH 44135, USA

[2]University of Toledo, Department of Mechanical Industrial & Manufacturing Engineering, Toledo, OH 43606, USA

(Received 19 September 2007 and in revised form 18 June 2008)

We consider a nominally uniform flow over a semi-infinite flat plate and show how a small slowly modulated (predominantly streamwise) disturbance of the upstream flow is amplified by leading-edge bluntness effects and eventually develops into a small-amplitude but nonlinear spanwise motion far downstream from the edge. This motion is then imposed on the viscous boundary layer at the surface of the plate – causing an order-one change in its profile shape, which can reduce the wall shear to zero and thereby causes the boundary layer to separate. The present study is similar to an earlier steady flow analysis, but the unsteady effects now cause the upstream boundary layer to develop inflectional profiles which can support rapidly growing inviscid instabilities that give rise to transition before the separation can occur.

1. Introduction

It is now understood that boundary-layer transition does not follow the classical Tollmien–Schlicting wave growth mechanism (sometimes referred to as natural transition) when the free-stream turbulence intensity is greater than about 1 %. Transition is then caused by the breakdown of elongated streamwise streaks, or Klebanoff modes, into turbulent spots when the turbulence level is not too high. Transition at even higher levels seems to take place by a different mechanism, which has been largely ignored by experimentalists, who usually dismiss it after noting that the turbulent spots appear to arise spontaneously in their experiments with no apparent precursors. Numerical studies of Nagarajan, Lele & Ferziger (2007, hereinafter referred to as NFL) suggest that this phenomenon may be considerably more complex than that – with the spots again evolving from a linear instability. However, unlike the lower-turbulence-level transition, leading-edge bluntness effects now seem to play an important role.

Investigations of leading-edge bluntness effects were carried out at low free-stream turbulence levels by Kendall (1991) and Watmuff (1997), who reported that changing the aspect ratio of the leading-edge ellipse seemed to affect the location of transition onset but had no observable affect on the Klebanoff-mode amplitude. However, the free-stream disturbance level was relatively low and the plates were fairly thin in these experiments. Klingmann *et al.* (1993) and Westin *et al.* (1994), who used an asymmetric leading edge to eliminate adverse pressure-gradient effects, found significant upstream movement of the transition onset location for slightly off-design conditions.

Goldstein, Leib & Cowley (1992, hereinafter referred to as GLC) showed that wake-like disturbances in the upstream flow (corresponding to wall normal vorticity) inviscidly stretch and tilt around the leading edge of the plate to produce enhanced streamwise vorticity which is then further amplified by the surface boundary layer when its spanwise length scale is of the order of the boundary-layer thickness. However, with the scaling used in that paper, the inviscid solution eventually develops a singularity that causes the viscous boundary layer to separate. The three-dimensional boundary-layer profiles remain non-inflectional everywhere upstream of the separation point and therefore, cannot support short-wavelength Rayleigh (i.e. inviscid) instabilities that grow on the inviscid time scale – which can be much shorter than the viscous time scale on which Tollmien–Schlicting waves grow. And the corresponding growth rates can then be much more rapid.

Goldstein & Leib (1993) considered the effect of weak streamwise vorticity in the upstream flow with the same asymptotic scaling. The leading-edge effects become insignificant in this model and only an infinitely thin plate was considered. They showed that this initially linear perturbation of the uniform upstream flow ultimately leads to a small-amplitude but nonlinear cross-flow far downstream of the leading edge which again causes the boundary layer to separate. The separation now occurs much further downstream allowing the upstream velocity profiles to become slightly inflectional. The resulting flow can then support rapidly growing Rayleigh instabilities that can break down into turbulent spots before the singularity develops. Goldstein (1997), following a suggestion of Kendall (personal communication), later proposed this as a paradigm of Klebanoff-mode transition and the Goldstein & Leib analysis (1993) was eventually extended to smaller turbulence Reynolds numbers by Wundrow & Goldstein (2001) in order to avoid the downstream singularity and to further investigate the secondary instability. The main conclusions of this latter paper are in qualitative agreement with the earlier high-Reynolds-number analysis of Goldstein & Leib (1993).

NFL used their numerical simulations to study the effects of leading-edge bluntness on boundary-layer transition. Their results seem to show that two different transition mechanisms can occur, depending on the free-stream turbulence level and amount of leading-edge bluntness. When they are low the transition appears to follow the Klebanoff mode paradigm discussed in Goldstein & Leib (1993), Goldstein (1997) and Wundrow & Goldstein (2001): formation of elongated streaks with spanwise length scale comparable to the boundary-layer thickness, local instability on the low-speed portion of the streak leading to turbulent spot formation. However, transition appears to take place by a somewhat different mechanism when the turbulence and bluntness are significantly higher. Wavepacket-like precursors to turbulent spots again appear to grow on the streak-like background disturbance inside the boundary layer and eventually dominate the motion; but overlaying the spot precursors on streaks suggested that the wave packets were not located on the low-speed streaks. NFL also point out that the wave packet precursors can be observed in their simulations only after they have undergone considerable growth.

Although the Goldstein & Leib (1993) and GLC analyses can explain the formation of low-speed streaks (i.e. velocity deficit portions of the boundary layer) neither of them can fully explain the numerical results found by NFL. The purpose of the present paper is to show that these results can be explained by extending the GLC analysis to include a slow unsteady modulation of the upstream wake-like disturbances. These modulations eventually cause the surface boundary layer to become fully unsteady and develop low-speed streaks that move across the layer. However, unlike the GLC case, the instantaneous streamwise velocity profiles can now become inflectional on the low-speed streaks and remain inflectional after the streak has moved to a new spanwise location – with the inflection point moving to the inner portion of the boundary layer once this has occurred.

Following Cowley (1985), Wu (1992) and Wu, Lee & Cowley (1993), we then show that wavepacket-like disturbances can grow rapidly on these inflectional profiles. Wave packets initiated on the streaks can become much larger than those initiated between the streaks, but reach their maximum amplitudes only after the low-speed streak has moved to its new transverse location. As usual the maximum disturbance amplitude tends to occur at the inflection point and the instability growth rate tends to decrease as the inflection point moves toward the wall. (The corresponding inviscid instability reduces to the type found by Wu & Choudhari, 2003 once it reaches the wall.) Our results show that the overall wave-packet growth is relatively small when the product of the upstream disturbance amplitude and the leading-edge thickness is large and is relatively large when this product is small. The wave packets are, therefore, likely to reach large amplitudes and become nonlinear when the local velocity profiles are still streak-like for thin plates and/or low free-stream turbulence levels but are unlikely to reach such amplitudes until the low-speed streaks have moved to a new location when the plate is sufficiently thick and/or the free-stream turbulence levels are sufficiently high.

Since the spot precursor wave packets in the NFL simulations may not have reached detectable amplitudes until the streaks had moved to a new location in the boundary layer when their plates were sufficiently thick and/or their free-stream turbulence levels were sufficiently high, this could explain why these packets appeared to grow on the turbulent streaks when either or both of these quantities were small and to grow on the relatively undisturbed area between the streaks when they were not. Since the streaks are forced to lie beneath the region of maximum free-stream vorticity for the simple upstream distortion imposed in our computations, this is consistent with NFL's observation that 'The spanwise profiles in figure 17(*d*) show the localized disturbance left behind by the [free stream] vortex pair, which has moved out of the frame. The spot precursor of figure 13(*d*) has a similar structure.' It is reasonable to expect that similar progressions occurred in the higher-turbulence-level experiments alluded to above – but with the spot forming before the precursors could reach observable amplitude. However, it should be emphasized that these conclusions are somewhat speculative because the present results are based on high-Reynolds-number asymptotics that may not apply at the more moderate Reynolds numbers of the simulations. But, the good qualitative agreement between the high-Reynolds-number analysis of Goldstein & Leib (1993) and the moderate-Reynolds-number Wundrow & Goldstein (2001) study lends considerable support to these inferences.

More specifically, the paper shows how small, slowly modulated, spanwise non-uniformities in the upstream velocity field can produce somewhat larger streamwise vorticity fields which can, in turn, produce significant (i.e. order-one) variations in the streamwise boundary-layer profiles. We assume that the characteristic dimension of the rounded leading edge is of the order of the spanwise length scale, say λ, of the upstream disturbance field, and that the Reynolds number based on λ, say R_λ, is large. Then the upstream distortion interacts linearly with the leading edge with the resulting inviscid flow being described well by the usual 'rapid distortion' theory (Goldstein 1978; Hunt & Carruthers 1990). The corresponding steady-flow analysis was, at least in principle, given by Lighthill (1956) who showed that the upstream distortion produces a spanwise velocity field that becomes logarithmically infinite at the surface of the body. This singularity must ultimately be removed by viscous effects, which (as in Toomre 1960) are confined to the viscous boundary layer (with the Reynolds-number amplitude scaling being considered herein). Our analysis shows that inviscid crossflow effects produce only a linear perturbation to the boundary-layer flow in the vicinity of the leading edge, where the undisturbed layer undergoes its most rapid streamwise development, but that they produce an order-one change in the mean boundary-layer profiles at large distances downstream where its streamwise development is on a considerably longer scale.

However, the linear rapid distortion-theory solution, which provides an adequate description of the external inviscid flow in the vicinity of the leading edge, breaks down at large streamwise distances, with the breakdown moving further upstream as the surface of the plate is approached. A new nonlinear solution then has to be obtained in order to describe the external inviscid flow in the physically interesting region where crossflow effects produce significant (i.e. order-one) changes in the boundary-layer profiles. The thickness of this nonlinear inviscid region is small compared to its streamwise dimension, but large compared to the boundary-layer thickness. It serves as a kind of 'blending layer' which connects the boundary-layer solution to the linear rapid-distortion-theory solution, which applies at an order-one (on the scale of λ) distance from the wall.

The blending-layer flow is governed by the inviscid Burgers equation (sometimes called the kinematic wave equation) whose solution eventually develops a singularity at a certain spanwise location and at a finite downstream position owing to the well-known wave-steepening effects associated with that solution. This also leads to a singularity (signified by the vanishing of the wall shear) in the boundary-layer flow at the same (spanwise and streamwise) location. This is similar to the chain of events described in the GLC paper, but the unsteady effects in the present analysis now cause the upstream boundary layer to develop inflectional profiles, which can support rapidly growing inviscid instabilities that give rise to transition before the separation can occur. The present work, therefore, focuses on the wave-packet growth that takes place on these profiles.

The overall plan of the paper is as follows. Section 2.1 describes the linear inviscid flow produced by the upstream distortion field and the initial breakdown of the relevant linear rapid-distortion theory solution is discussed in § 2.2. The appropriate nonlinear, but inviscid, solution that eliminates this breakdown is described in § 3.

The viscous boundary-layer problem is formulated in § 4 and its numerical solution is described in § 5. The results show that the boundary layer develops streamwise streaks (i.e. elongated regions of low-speed flow) and inflectional streamwise velocity profiles that can support linear wave-packet growth.

The wave-packet solutions are constructed in § 6.1. The phase of these packets is found by solving a first-order nonlinear partial differential equation obtained from the local dispersion relation of an appropriate Rayleigh equation. Section 6.2 describes the initial-value problem for that equation and its numerical solution is discussed in § 6.3. Section 7 summarizes the main findings of this work and discusses the physical implications of the numerical results.

2. Formulation and breakdown of linear solution

We are concerned with the flow over a semi-infinite flat plate of finite thickness h^* with leading-edge ellipse of dimension $O(h^*)$. The upstream flow is assumed to be nominally uniform, except for a small $O(\varepsilon)$ purely convected perturbation, say $U_\infty \boldsymbol{u}_\infty$, which has a transverse length scale $\lambda = O(h^*)$ and is assumed to depend on the time and streamwise coordinate only through the slow variables

$$\bar{x} \equiv \varepsilon\,\bar{a}x/\sigma, \quad \bar{t} \equiv \varepsilon\,\bar{a}t/\sigma, \tag{2.1}$$

where the three parameters $\varepsilon \ll \sigma \ll 1$ and $\bar{a} = O(1)$ will be specified below. It must, therefore, be of the form

$$\boldsymbol{u}_\infty = \left\{ u_\infty(\bar{x}-\bar{t}, \boldsymbol{x}_\perp), \frac{\varepsilon}{\sigma}\bar{a}\,\bar{v}_\infty(\bar{x}-\bar{t}, \boldsymbol{x}_\perp), \frac{\varepsilon}{\sigma}\bar{a}\,\bar{w}_\infty(\bar{x}-\bar{t}, \boldsymbol{x}_\perp) \right\}, \tag{2.2}$$

in order to satisfy the continuity equation

$$\nabla \cdot \boldsymbol{u}_\infty = \frac{\partial u_\infty}{\partial \bar{x}} + \frac{\partial \bar{v}_\infty}{\partial y} + \frac{\partial \bar{w}_\infty}{\partial z} = 0, \tag{2.3}$$

where

$$\boldsymbol{x}_\perp \equiv \{0, y, z\}, \tag{2.4}$$

and we are assuming that all lengths are normalized by λ, the time t by λ/U_∞ and the velocity $\boldsymbol{u} = \{u, v, w\}$ by the uniform upstream mean flow velocity U_∞. The flow is assumed to be incompressible, with density ρ and the pressure p is normalized by ρU_∞^2. The plate thickness h^* is, for simplicity, taken to be $O(\lambda)$, and the x-coordinate is assumed to be in the streamwise direction with the origin at the leading edge while the origin of the y-coordinate coincides with the flat surface of the plate far downstream in the flow.

Finally, we require that the Reynolds number $R_\lambda = U_\infty\lambda/\nu$, where ν is the kinematic viscosity, be large enough to ensure that the viscous effects are initially confined to a thin boundary layer at the surface of the plate which is predominantly two-dimensional near the forward stagnation point. This will occur (and the boundary layer will then remain thin until nonlinear effects influence the external motion downstream in the flow) if

$$\ln R_\lambda \ll \frac{1}{\varepsilon} \ll R_\lambda, \tag{2.5}$$

which is satisfied reasonably well by the typical values of $R_\lambda \sim 5000$ and $\varepsilon \sim 0.05$ in the NFL simulation.

2.1. *The linear solution*

Then the entire flow will be nearly two-dimensional in the vicinity of the leading edge, i.e. in the region where $x = O(1)$, with the three-dimensional effects being an $O(\varepsilon)$ perturbation of the two-dimensional base flow, say $\{U_0(x, y), V_0(x, y), 0\}$. Since the viscous effects are confined to a thin region whose thickness is $O(R_\lambda^{-1/2})$, the solution outside this region should expand as

$$\begin{aligned} \boldsymbol{u} &= \{U_0,\ V_0,\ 0\} + \varepsilon\{\tilde{u}_0, \tilde{v}_0, \tilde{w}_0\} + \varepsilon^2\{u_1, v_1, w_1\} + \cdots \\ &= \{U_0,\ V_0,\ 0\} + \varepsilon\,\tilde{\boldsymbol{u}}_0 + \varepsilon^2 \boldsymbol{u}_1 + \cdots, \end{aligned} \tag{2.6}$$

$$p = P_0 + \varepsilon\,\tilde{p}_0 + \varepsilon^2 p_1 \ldots, \tag{2.7}$$

where $\tilde{\boldsymbol{u}}_0$ and $\tilde{p}_0$ can depend on ε/σ.

The analysis in this and the following subsection is very similar to, but slightly more complicated than, that of GLC, and, as in that reference, the complex conjugate mean flow velocity $\zeta = U_0 - \mathrm{i}V_0$ (which is assumed to include the $O(R_\lambda^{-1/2})$ boundary-layer displacement effects) is an analytic function of $Z \equiv x + \mathrm{i}[y + (h*/\lambda)]$ that can be expressed in terms of a complex potential, say

$$\tilde{W} = \Phi + \mathrm{i}\Psi, \tag{2.8}$$

where Φ is the velocity potential and Ψ is the streamfunction, in the usual way by

$$\varsigma = \frac{\mathrm{d}\tilde{W}}{\mathrm{d}Z}. \tag{2.9}$$

For definiteness, we suppose that $\Psi = 0$ on the surface of the (body) plate and along the stagnation streamline, and that $\Phi \to 0$ at the forward stagnation point.

The first-order perturbations are governed by the linearized Euler equations and the decomposition introduced in Goldstein (1978; also see Goldstein 1979) can be used to show that the relevant solution is determined by

$$\tilde{\boldsymbol{u}}_0 = \nabla\tilde{\phi}_0 + \tilde{\boldsymbol{u}}^{\boldsymbol{I}}, \tag{2.10}$$

where

$$\tilde{\boldsymbol{u}}^{\boldsymbol{I}} = u_\infty(\bar{\Delta} - \bar{t}, \boldsymbol{X}_\perp)\nabla\Delta + \frac{\varepsilon}{\sigma}\bar{a}[\bar{v}_\infty(\bar{\Delta} - \bar{t}, \boldsymbol{X}_\perp)\nabla\Psi + \bar{w}_\infty(\bar{\Delta} - \bar{t}, \boldsymbol{X}_\perp)\hat{\boldsymbol{k}}], \tag{2.11}$$

$$\bar{\Delta} \equiv \varepsilon\bar{a}\Delta/\sigma, \quad \boldsymbol{X}_\perp \equiv \{0, \Psi, z\}, \tag{2.12}$$

$\hat{\boldsymbol{k}}$ denotes the unit vector in the z-direction, the Lighthill (1956)–Darwin (1954) drift function,

$$\Delta \equiv \Phi + \int_{-\infty}^{\Phi}\left[\frac{1}{U_0^2(\Psi, \tilde{\Phi}) + V_0^2(\Psi, \tilde{\Phi})} - 1\right]\mathrm{d}\tilde{\Phi}, \tag{2.13}$$

and the Lagrangian coordinate $\boldsymbol{X}_\perp$ behave as

$$\left.\begin{aligned} &\Delta \to x + O(x^{-1}) \text{ as } x \to -\infty,\ \Delta \to x + \Delta_+(y) + O(x^{-1}), \text{ as } x \to \infty, \\ &\qquad\qquad \boldsymbol{X}_\perp \to \boldsymbol{x}_\perp + O(x^{-1}),\ x \to \pm\infty. \end{aligned}\right\} \tag{2.14}$$

The potential $\tilde{\phi}_0$, which is related to the pressure by

$$\tilde{p}_0 = -\left(U_0\frac{\partial}{\partial x} + V_0\frac{\partial}{\partial y}\right)\tilde{\phi}_0, \tag{2.15}$$

is determined by

$$\begin{aligned} \nabla^2\tilde{\phi}_0 = -\nabla\cdot(\tilde{\boldsymbol{u}}^{\boldsymbol{I}}) &= -\nabla\cdot[u_\infty(\bar{\Delta} - \bar{t}, \boldsymbol{X}_\perp)\nabla\Delta] \\ &\quad - \frac{\varepsilon}{\sigma}\bar{a}\nabla\cdot[\bar{v}_\infty(\bar{\Delta} - \bar{t}, \boldsymbol{X}_\perp)\nabla\Psi + \bar{w}_\infty(\bar{\Delta} - \bar{t}, \boldsymbol{X}_\perp)\hat{\boldsymbol{k}}], \end{aligned} \tag{2.16}$$

and, finally, the normal component of $\tilde{\boldsymbol{u}}_0$ must vanish at the surface of the plate.

2.2. *Breakdown of the linear solution*

The expansions (2.6) and (2.7) are non-uniform in the vicinity of the plate since (2.10) to (2.13) and the results of the Appendix in GLC show that the spanwise velocity $\tilde{w}_0$ becomes infinite there as

$$\tilde{w}_0 \to \bar{a}\, u'_{\infty,0}(\bar{x} - \bar{t}, z)\ln\Psi + O(1) \text{ as } \Psi \to 0, \tag{2.17}$$

where

$$u_{\infty,0}(\bar{x} - \bar{t}, z) \equiv u_\infty(\bar{x} - \bar{t}, \boldsymbol{x}_\perp)|_{y=0}, \tag{2.18}$$

the leading-edge bluntness parameter $\bar{a}$ (which is related to the local potential flow behaviour in the vicinity of the forward stagnation point) is the reciprocal of the parameter a used in GLC and the prime denotes differentiation with respect to z.

As in GLC, the stagnation-line non-uniformity can be ignored because the linearized equations give the correct solution (to the order of interest here) right up to the edge of the viscous boundary layer. Another, much more important, non-uniformity develops far downstream in the flow where x becomes large and, as noted in GLC,

$$\Psi \to y, \quad U_0 \to 1, \quad \Phi \to x + O(1), \quad \Delta \to \Delta_+(y) + x + O(x^{-1}), \tag{2.19}$$

where

$$\Delta_+(y) = \int_{-\infty}^{\infty} \left(\frac{1}{U_0^2 + V_0^2} - 1 \right) \mathrm{d}\Phi \to \Delta_0(y) - \bar{a} \ln y \ \text{ as } \ y \to 0 \tag{2.20}$$

with Δ_0 remaining bounded as $y \to 0$. It, therefore, follows from (2.16) that

$$\begin{aligned} \nabla^2 \tilde{\phi}_0 \to & -\frac{\partial}{\partial y} u_\infty \left(\bar{x} - \bar{t} + \frac{\varepsilon}{\sigma} \bar{a}\, \Delta_+, \boldsymbol{x}_\perp \right) \Delta'_+(y) \\ & - \frac{\varepsilon}{\sigma} \bar{a} \frac{\partial}{\partial y} \bar{v}_\infty \left(\bar{x} - \bar{t} + \frac{\varepsilon}{\sigma} \bar{a}\, \Delta_+, \boldsymbol{x}_\perp \right) + O(x^{-1}) \, \text{as}\, x \to \infty. \end{aligned} \tag{2.21}$$

These equations along with (2.10) and (2.14) suggest that $\tilde{\phi}_0$, $\tilde{p}_0$ and $\tilde{\boldsymbol{u}}_0$ be re-expanded as

$$\tilde{\phi} + \frac{\varepsilon}{\sigma} \bar{a}\, \tilde{\phi}_1 \equiv \tilde{\phi}_0 + \int u_\infty (\bar{x} - \bar{t}, \boldsymbol{x}_\perp)\, \Delta'_+ (y)\, \mathrm{d}y, \tag{2.22}$$

$$\left. \begin{aligned} \tilde{\boldsymbol{u}}_{\boldsymbol{0}} \to \{u_0, v_0, w_0\} + \frac{\varepsilon}{\sigma} \bar{a} \{u_{0,1}, v_{0,1}, w_{0,1}\} = \boldsymbol{u}_0 + \frac{\varepsilon}{\sigma} \bar{a} \boldsymbol{u}_{0,1}, \\ \tilde{p}_0 \to p_0 + \frac{\varepsilon}{\sigma} \bar{a}\, p_{0,1}, \end{aligned} \right\} \tag{2.23}$$

when x becomes large. Appendix A shows that

$$\left. \begin{aligned} \nabla^2 \tilde{\phi} &= \frac{\partial^2}{\partial z^2} \int u_\infty (\bar{x} - \bar{t}, \boldsymbol{x}_\perp)\, \Delta'_+ (y)\, \mathrm{d}y, \\ \nabla^2 \tilde{\phi}_1 &= - \left[\frac{\partial}{\partial \bar{x}} u_\infty (\bar{x} - \bar{t}, \boldsymbol{x}_\perp)\, \Delta'_+ (y)\, \Delta_+ (y) + \bar{v}_\infty \left(\bar{x} - \bar{t} + \frac{\varepsilon}{\sigma} \bar{a} \Delta_+, \boldsymbol{x}_\perp \right) \right], \end{aligned} \right\} \tag{2.24}$$

that $\tilde{\phi}$ becomes independent of x and, therefore, that (see (2.15))

$$\begin{aligned} \boldsymbol{u}_0 &= \left\{ u_\infty (\bar{x} - \bar{t}, \boldsymbol{x}_\perp), \frac{\partial \tilde{\phi}}{\partial y}, \frac{\partial \tilde{\phi}}{\partial z} - \frac{\partial}{\partial z} \int u_\infty (\bar{x} - \bar{t}, \boldsymbol{x}_\perp)\, \Delta'_+ (y)\, \mathrm{d}y \right\}, \\ \boldsymbol{u}_{0,1} &= \left\{ \frac{\partial}{\partial \bar{x}} \left[\tilde{\phi}_1 + \int \Delta_+ (y) \frac{\partial}{\partial y} u_\infty (\bar{x} - \bar{t}, \boldsymbol{x}_\perp)\, \mathrm{d}y \right], \right. \\ & \qquad \left. \frac{\partial \tilde{\phi}_1}{\partial y} + \bar{v}_\infty (\bar{x} - \bar{t}, \boldsymbol{x}_\perp), \frac{\partial \tilde{\phi}_1}{\partial z} + \bar{w}_\infty (\bar{x} - \bar{t}, \boldsymbol{x}_\perp) \right\}, \end{aligned} \tag{2.25}$$

$$p_0 = 0. \tag{2.26}$$

It can now be seen that the normal component of $\boldsymbol{u}_0$ will vanish at the plate if

$$\frac{\partial \tilde{\phi}}{\partial y} = 0 \ \text{ at } \ y = 0, \tag{2.27}$$

and that

$$\tilde{\phi} \to \beta (\bar{x} - \bar{t}, z) - \bar{a}\, u''_{\infty,0} (\bar{x} - \bar{t}, z) \frac{y^2}{2} \ln y + O(y^2) \quad \text{as } y \to 0, \tag{2.28}$$

$$\tilde{\phi}_1 \to \beta_1 (\bar{x} - \bar{t}, z) - \bar{a}^2 \frac{\partial^2 u''_{\infty,0} (\bar{x} - \bar{t}, z)}{\partial \bar{x}^2} \frac{y}{2} \ln^2 y + O\,(y \ln y) \quad \text{as } y \to 0. \tag{2.29}$$

Substituting (2.6) and (2.7) into Euler's equations and using the second member of (2.14) along with (2.17) shows that

$$\begin{aligned}\frac{\partial \boldsymbol{u}_1}{\partial x} &+ \nabla p_1 \rightarrow -\boldsymbol{u}_0 \cdot \nabla \boldsymbol{u}_0 \rightarrow \\ &- \left[\tilde{\phi}_y \frac{\partial}{\partial y} + \left(\tilde{\phi}_z - \int \frac{\partial}{\partial z} u_\infty (\bar{x} - \bar{t}, \boldsymbol{x}_\perp)\, \Delta'_+ (y)\, \mathrm{d}y\right) \frac{\partial}{\partial z}\right] \\ &\times \left\{u_\infty (\bar{x} - \bar{t}, \boldsymbol{x}_\perp), \tilde{\phi}_y, \tilde{\phi}_z - \frac{\partial}{\partial z} \int u_\infty (\bar{x} - \bar{t}, \boldsymbol{x}_\perp)\, \Delta'_+ (y)\, \mathrm{d}y\right\}, \end{aligned} \tag{2.30}$$

where the term in square brackets is a linear operator. So introducing the change in variable

$$\boldsymbol{x}, t \rightarrow \boldsymbol{x}, \tau \equiv t - x, \tag{2.31}$$

putting

$$\bar{\tau} \equiv \frac{\varepsilon}{\sigma} \bar{a}\, (t - x) = \bar{t} - \bar{x} \tag{2.32}$$

and using (2.20), (2.28) and (2.29) now shows that the first-order perturbation $\boldsymbol{u}_1$, p_1 satisfies (2.20) to (2.23) of GLC with $u_{\infty}(z)$ replaced by $u_{\infty,0}(\bar{\tau}, z)$ when $y \rightarrow 0$, $x \rightarrow \infty$, which means that the variable $\bar{\tau}$ enters only parametrically in this region. (Recall that $\bar{a}$ is the reciprocal of the parameter a in GLC.) Since (2.20) implies that

$$\frac{\partial}{\partial z} \int u_\infty (\bar{x} - \bar{t}, \boldsymbol{x}_\perp)\, \Delta'_+ (y)\, \mathrm{d}y \rightarrow -\bar{a} \ln y\, u'_{\infty,0}(\bar{\tau}, z) \text{ as } y \rightarrow 0, \tag{2.33}$$

it follows from (2.6), (2.7), (2.17), (2.19), (2.25), (2.26) and arguments given near the end of § 2.2 of GLC, that u, w, p satisfy (2.26) to (2.28) of GLC with $d\,(z)$ replaced by $d\,(\bar{\tau}, z)$ when $y \rightarrow 0$ and $x \rightarrow \infty$ and that that expansion again breaks down when

$$-\varepsilon \bar{a}\, x \ln y = O\,(1)\,. \tag{2.34}$$

3. Blending-layer solution

Then since the solution in the region (2.34), which we refer to as the 'blending layer', is completely determined by the initial conditions (2.26) to (2.28) of GLC, the analysis of § 3 of GLC where the new gauge functions $\sigma(\varepsilon)$ and $\delta(\varepsilon)$ (see also (4.11))

$$\sigma\,(\varepsilon) = -\frac{1}{\ln \delta\,(\varepsilon)} \rightarrow 0 \text{ as } \varepsilon \rightarrow 0, \tag{3.1}$$

along with the new scaled variables

$$\bar{x} \equiv \frac{\varepsilon\, \bar{a}\, x}{\sigma} \tag{3.2}$$

and

$$\eta \equiv -\sigma \ln y = \frac{\ln y}{\ln \delta}, \tag{3.3}$$

are introduced, applies to the present problem as well. The important results are that the pressure and cross-stream velocities in this region are now given by

$$p = \varepsilon^2 \mathrm{d}\,(\bar{\tau}, z) + \frac{1}{2} \left(\frac{\varepsilon}{\sigma} \bar{a}\, \mathrm{e}^{-\eta/\sigma}\right)^2 [\eta^2 \bar{p}_0\,(\bar{\tau}, \xi, z) + \sigma\, \eta\, \bar{p}_1\,(\bar{\tau}, \xi, z) + O(\sigma^2)], \tag{3.4}$$

$$v = \frac{\varepsilon}{\sigma} \bar{a}\, \mathrm{e}^{-\eta/\sigma} [\eta \bar{v}_0\,(\bar{\tau}, \xi, z) + \sigma\, \bar{v}_1\,(\bar{\tau}, \xi, z) + O(\sigma^2)], \tag{3.5}$$

$$w = \frac{\varepsilon}{\sigma} \bar{a} [\eta \bar{w}_0\,(\bar{\tau}, \xi, z) + \sigma\, \bar{w}_1\,(\bar{\tau}, \xi, z) + O(\sigma^2)], \tag{3.6}$$

where

$$\xi \equiv \bar{x}\eta, \tag{3.7}$$

$$\left(\frac{\partial \bar{w}_0}{\partial z}\right)^2 = \bar{v}_0^2 = -\bar{p}_0/2, \tag{3.8}$$

and the spanwise velocity

$$\bar{w}_0 = g\,(\bar{\tau}, z - \bar{w}_0\xi)\,, \tag{3.9}$$

with g given by

$$g\,(\bar{\tau}, z) = -u'_{\infty,0}\,(\bar{\tau}, z)\,, \tag{3.10}$$

and the variable $\bar{\tau}$ again entering only parametrically, will usually develop a singularity at a finite value, say $\xi = \xi_s$, of ξ.

Equations (3.3) and (3.7) show that $\xi = \bar{x}\,(1 - \sigma \ln Y)$, where

$$Y \equiv \frac{y}{\delta}, \tag{3.11}$$

so that (3.9) becomes

$$\bar{w}_0 = g\,(\bar{\tau}, z - \bar{x}\;\bar{w}_0) \tag{3.12}$$

in the 'small' sublayer $Y = O(1)$ of the much thicker region $\eta = O(1)$.

4. The boundary-layer expansion

4.1. *The quasi-steady linear region*

Viscous effects must come into play when y becomes sufficiently small. The resulting boundary layer will initially be two-dimensional with the spanwise variations producing only a linear perturbation of the Blasius flow when $1 \ll x \ll \sigma/\bar{a}\,\varepsilon$. In which case, it follows from (3.6) and (3.9) that the relevant solution is given by (Crow 1966)

$$u = F'(\eta_B) + \frac{\varepsilon}{2\sigma}\bar{a}\,g'(\bar{\tau}, z)x\eta_B F''(\eta_B) + \cdots\,, \tag{4.1}$$

$$v = \frac{1}{\sqrt{2R_\lambda x}}\left\{\eta_B F'(\eta_B) - F(\eta_B)\right.$$
$$\left. + \frac{\varepsilon\bar{a}\,x}{2\sigma}\left[\eta_B^2 F''(\eta_B) - 3\eta_B F'(\eta_B) - F(\eta_B)\right]\,g'(\bar{\tau}, z) + \cdots\right\}, \tag{4.2}$$

$$w = \frac{\varepsilon}{\sigma}\bar{a}g'(\bar{\tau}, z)F'(\eta_B) + \cdots\,, \tag{4.3}$$

where the primes denote differentiation with respect to z or η_B as appropriate, $\eta_B = O(1)$ denotes the Blasius variable

$$\eta_B = y\sqrt{\frac{R_\lambda}{2x}}, \tag{4.4}$$

$F\,(\eta_B)$ satisfies the Blasius equation

$$F''' + FF'' = 0, \tag{4.5}$$

$$F(0) = F'(0) = 0, \tag{4.6}$$

$$F \rightarrow \eta_B - \beta, \quad \eta_B \rightarrow \infty, \tag{4.7}$$

and $\beta \cong 1.217\cdots$.

4.2. *The fully unsteady nonlinear region*

The expansions (4.1) to (4.3) clearly break down when $\bar{x} \equiv \varepsilon\bar{a}x/\sigma = O(1)$ and a new expansion must be obtained for this region. The distinguished scaling corresponds to identifying the length scale $\lambda\delta$ introduced in § 3 with the boundary-layer thickness $\sqrt{2x/R_\lambda}$. We, therefore, suppose that $Y = O(1)$, introduce the long streamwise length scale

$$L^* = \frac{\lambda}{\varepsilon\bar{a}\ln(1/\delta)}, \tag{4.8}$$

and set

$$\lambda\delta = L^*/R^{1/2}, \tag{4.9}$$

where

$$R \equiv \frac{U_\infty L^*}{\nu} \tag{4.10}$$

is the global Reynolds number based on L^*. It then follows that

$$\delta = (R_\lambda \varepsilon\,\bar{a}\ln[1/\delta])^{-1/2}, \tag{4.11}$$

which, in view of (2.5), is consistent with our assumption (3.1) that $\delta \ll 1$. We only consider the region where $|\bar{x} - \xi_s| \gg \sigma$ in this paper (ξ_s is defined below (3.10)).

We expect the streamwise velocity

$$u = U(\bar{t}, \bar{x}, Y, z) \tag{4.12}$$

to be $O(1)$ in this part of the flow, and in order to satisfy continuity we put

$$v = -\varepsilon\,\bar{a}\delta(\ln\delta)V, \tag{4.13}$$

$$w = -\varepsilon\,\bar{a}(\ln\delta)W, \tag{4.14}$$

where V and W are, of course, assumed to remain $O(1)$ as $\varepsilon \to 0$. Equations (3.3), (3.4) and (3.18) suggest that

$$p = \varepsilon^2 \mathrm{d}(\bar{\tau}, z) + O(\varepsilon\,\bar{a}\delta\ln\delta)^2 \tag{4.15}$$

in this region.

Substituting these scalings into the Navier–Stokes equations yields the unsteady three-dimensional zero-pressure-gradient boundary-layer equations

$$\frac{\partial U}{\partial\bar{t}} + U\frac{\partial U}{\partial\bar{x}} + V\frac{\partial U}{\partial Y} + W\frac{\partial U}{\partial z} = \frac{\partial^2 U}{\partial Y^2}, \tag{4.16}$$

$$\frac{\partial W}{\partial\bar{t}} + U\frac{\partial W}{\partial\bar{x}} + V\frac{\partial W}{\partial Y} + W\frac{\partial W}{\partial z} = \frac{\partial^2 W}{\partial Y^2}, \tag{4.17}$$

$$\frac{\partial U}{\partial\bar{x}} + \frac{\partial V}{\partial Y} + \frac{\partial W}{\partial z} = 0, \tag{4.18}$$

and U must clearly go to unity as $Y \to \infty$ in order to match with (3.7) of GLC. The boundary condition for W is a little more subtle. The known properties of the boundary-layer solutions suggest that the normal derivatives should become small as $Y \to \infty$. Equation (4.17) therefore becomes

$$\frac{\partial W}{\partial\bar{t}} + \frac{\partial W}{\partial\bar{x}} + W\frac{\partial W}{\partial z} = 0, \tag{4.19}$$

whose solution is given by

$$W = G(\bar{t} - \bar{x}, z - \bar{x}W). \tag{4.20}$$

This will clearly agree with (3.9) and (4.14), and will therefore match with (3.3) and (3.6) if we take

$$G = g, \tag{4.21}$$

where g is given by (3.10). It is worth noting that the continuity equation (4.18) automatically ensures that (4.13) will match with (3.5) and (3.8).

The appropriate boundary conditions for (4.16)–(4.18) are therefore

$$U \to 1, \quad W \to g(\bar{t} - \bar{x}, z - \bar{x}W) \quad \text{as } Y \to \infty, \tag{4.22}$$

$$U = V = W = 0 \quad \text{at } Y = 0, \tag{4.23}$$

and since it follows from (2.1), (3.1), (3.11), (4.4) and (4.11) that

$$\eta_B = Y/\sqrt{2\bar{x}}, \tag{4.24}$$

matching with the upstream solution (4.1)–(4.3) requires that

$$U \to F'(\eta_B) + \tfrac{1}{2} g'(\bar{\tau}, z)\bar{x}\eta_B F''(\eta_B), \tag{4.25}$$

$$V \to \frac{1}{\sqrt{2\bar{x}}}[\eta_B F'(\eta_B) - F(\eta_B)] + \frac{\sqrt{2\bar{x}}}{4}\left[\eta_B^2 F''(\eta_B) - 3\eta_B F'(\eta_B) - F(\eta_B)\right] g'(\bar{\tau}, z) \tag{4.26}$$

and

$$W \to g'(\bar{\tau}, z)F'(\eta_B) \tag{4.27}$$

as $\bar{x} \to 0$. The solution to this problem should become singular at the inviscid singular point ξ_s.

5. Numerical solution of the boundary-layer problem

The full unsteady problem (4.16)–(4.18) and (4.22)–(4.27) depends on the upstream distortion only through the function $g(\bar{\tau}, z)$ defined by (2.18), (2.32) and (3.10). The steady-state solution to this problem is expected to be independent of initial conditions when the upstream forcing is periodic (as it is in the present computations). However, the numerical procedure is most conveniently implemented by solving an initial-value problem and running the calculation until the steady state is reached. The initial condition was taken to be the steady flow obtained by setting $\bar{t} = 0$, or equivalently $\bar{\tau} = -\bar{x}$, in the upstream distortion function $g(\bar{\tau}, z)$. This latter quantity can then be set equal to zero in the upstream boundary condition (4.25)–(4.27) for the upstream distortion (7.1) used in the calculations, since $g(0, z) = 0$ in that case. The resulting steady flow was calculated by solving the boundary-layer problem as formulated in GLC with $\bar{t}$ set equal to zero in the transverse boundary condition (4.22). More specifically, the solution was obtained by using the Keller box method (Keller & Cebeci 1972; Cebeci & Smith 1974; Cebeci, Khattab & Stewartson 1981), which is a finite-difference procedure that advances the solution in $\bar{x}$ and z from given initial conditions and an independent symmetry-plane calculation. The marching in z can proceed from the symmetry plane at $z = -\pi$ to the one at $z = 0$ once the distortion function $g(-\bar{x}, z)$ is selected. The standard box (Cebeci *et al.* 1981) was found to be adequate in the absence of any spanwise flow reversal.

The full three-dimensional unsteady boundary-layer problem (4.16)–(4.18) and (4.22)–(4.27) was rewritten in terms of the stretched Blasius variable (4.24) and the new dependent variable

$$e \equiv -V\sqrt{2\bar{x}} + \eta_B U, \tag{5.1}$$

to obtain

$$\frac{\partial U}{\partial \bar{t}} + U\frac{\partial U}{\partial \bar{x}} + W\frac{\partial U}{\partial z} = \frac{1}{2\bar{x}}\left(\frac{\partial^2 U}{\partial \eta_B^2} + e\frac{\partial U}{\partial \eta_B}\right), \tag{5.2}$$

$$\frac{\partial W}{\partial \bar{t}} + U\frac{\partial W}{\partial \bar{x}} + W\frac{\partial W}{\partial z} = \frac{1}{2\bar{x}}\left(\frac{\partial^2 W}{\partial \eta_B^2} + e\frac{\partial W}{\partial \eta_B}\right), \tag{5.3}$$

$$\frac{\partial U}{\partial \bar{x}} + \frac{\partial W}{\partial z} = \frac{1}{2\bar{x}}\left(\frac{\partial e}{\partial \eta_B} - U\right), \tag{5.4}$$

where

$$U \to 1, \quad W \to g(\bar{t} - \bar{x}, z - \bar{x}W) \quad \text{as } \eta_B \to \infty, \tag{5.5}$$

$$U = e = W = 0 \quad \text{at} \quad \eta_B = 0, \tag{5.6}$$

and

$$U \to F'(\eta_B) + \tfrac{1}{2}g'(\bar{\tau}, z)\bar{x}\eta_B F''(\eta_B), \tag{5.7}$$

$$e \to F(\eta_B) + \bar{x}\left(\eta_B^2 F''(\eta_B) - \tfrac{3}{2}\eta_B F'(\eta_B) - \tfrac{1}{2}F(\eta_B)\right)g'(\bar{\tau}, z), \tag{5.8}$$

$$W \to g'(\bar{\tau}, z)F'(\eta_B), \tag{5.9}$$

as $\bar{x} \to 0$, with periodic boundary conditions being imposed in the spanwise direction.

This transformed problem was solved using the dual-time-stepping technique (Jameson 1991; Gaitonde 1998), which involves modifying the governing equations to include terms that are unsteady in a fictitious pseudotime. Solutions of the modified equations that are steady in pseudotime are identical to the instantaneous unsteady solutions of the original equations (5.2)–(5.9) in physical time. The pseudotime marching was carried out using a four-stage Runge–Kutta scheme (Jameson, Schmidt & Turkel 1981).

The domain extended from 0 to 0.8 in the streamwise direction, from 0 to 8 in the cross-stream direction and from $-\pi/2$ to $3\pi/2$ in the spanwise direction to include two singularity locations. A three-dimensional Cartesian grid was built with 24, 80 and 80 points along the $\bar{x}$-, η_B- and z-directions, respectively. The number of grid points was set by using a grid-convergence analysis. Several grid configurations (corresponding to different numbers of grid points) were tested until an accurate result was obtained. The accuracy was measured by the difference between the flow variable averages (over the entire grid) calculated on two different grid configurations. For example, the average $U_i^1$of the dependent variable U over all grid points $i = 1, N_{T_1}$, in configuration 1 with the number of grid points equal to N_{T_1}, was calculated from

$$\langle U^1 \rangle = \frac{1}{N_{T_1}}\sum_{i=1}^{N_{T_1}} U_i^1. \tag{5.10}$$

The maximum acceptable value of the difference,

$$\varepsilon^* \equiv |\langle U^2 \rangle - \langle U^1|, \tag{5.11}$$

between the numerical results for the grid configurations 1 and 2 was set equal to 10^{-4}. The analysis was repeated for every dependent variable.

The grid was stretched along the η_B-direction, near the wall, and along the z-direction, in the vicinity of the inviscid singularities. All the spatial derivatives in (5.2)–(5.4) were discretized at the new time level, $n + 1$, to obtain an unconditionally stable scheme. The derivatives with respect to η_B were replaced with second-order centred finite differences and (unexpected) spurious numerical waves produced by (5.4), which does not include second derivatives, were eliminated by the inclusion of filtering terms (Kennedy & Carpenter 1994). The x derivatives and the time derivatives were discretized using backward finite-difference schemes of second order, except at the first point–where, first-order backward schemes were used. The spanwise convection terms, i.e. $W\partial U/\partial z$ and $W\partial W/\partial z$, were replaced with a second-order upwind approximation in order to deal with local region of reverse cross-flow that can occur in the boundary layer.

Equations (5.2)–(5.4) can then be written as

$$\mathrm{R}(Q^{n+1}, Q^n) = 0, \tag{5.12}$$

where the operator R is called unsteady residual, and $Q = [U\ W\ e]^T$ is the vector of dependent variables. The dual-time-stepping technique replaces this by the equation

$$\frac{\partial Q^{n+1}}{\partial \hat{t}} + R(Q^{n+1}, Q^n) = 0, \tag{5.13}$$

which is integrated until the derivative with respect to $\hat{t}$ goes to zero using the four-stage Runge–Kutta marching technique (Jameson *et al.* 1981) in pseudotime $\hat{t}$. The resulting Q vector is the unsteady solution of (5.2)–(5.4) at the $n+1$ physical time level.

A discrete l^2-norm, which approximates the integral L^2-norm, was used to evaluate the error involved in the numerical integration of (5.13). More specifically, the l^2-norm of the vector containing the elements

$$\varepsilon_i^U = \{U_i^{\nu+1} - U_i^{\nu}, \quad i = 1, \quad N_T\} \tag{5.14}$$

where N_T is the total number of grid points and ν indexes the dual-time level, is given by

$$\|\varepsilon^U\|_2 = \sqrt{\sum_{i=1}^{N_T} |U_i^{\nu+1} - U_i^{\nu}|^2}. \tag{5.15}$$

Equation (5.13) was deemed to be converged to (5.12) when all of the l^2-norms $\|\varepsilon^U\|_2$, $\|\varepsilon^W\|_2$ and $\|\varepsilon^e\|_2$ corresponding to the dependent variables U, W and e, respectively, were smaller than 10^{-6}.

6. Wave-packet solution

6.1. *Construction of solution*

We begin by supposing that a two-dimensional free-stream disturbance (such as a blob of turbulence), which varies on the 'fast' length and time scales

$$X, Y, Z, T \equiv x/\delta,\ y/\delta,\ z/\delta,\ t/\delta, \tag{6.1}$$

inserts itself into the boundary layer in some reasonably small neighbourhood of X_0, Z_0, T_0. The velocity $U(\bar{t}, \bar{x}, Y, z)$ can be considered to be a locally parallel two-dimensional quasi-steady mean flow, since it changes much more rapidly with respect to the unscaled variable y than it does relative to the unscaled variables x, z, t in the limit as $\varepsilon/\sigma \to 0$ (Cowley 1985; Wu 1992; Wu *et al.* 1993). While the wave packets are clearly three-dimensional in the NFL simulation, we shall, for simplicity, consider only the two-dimensional case. This amounts to assuming that the spanwise length scale of the disturbance is much larger than its streamwise length scale, but much smaller than the spanwise length scale of the mean flow, which is possible because the spanwise scale of the base flow is large compared to the streamwise scale of the disturbance.

The straightforward local solution to the incompressible linearized Navier–Stokes equations (about the velocity $\{U, V, W\}$) that varies in space and time on the fast scales X, Y, T, therefore, possess an expansion of the form

$$v(X, Y, T; \varepsilon/\sigma) = v_0(X, Y, T) + (\varepsilon\, \delta\, \bar{a}/\sigma) v_1(X, Y, T) + \cdots, \tag{6.2}$$

with the lowest-order term being given by the initial-value-problem solution

$$v_0(X, Y, T) = \int_{-\infty+\mathrm{i}c}^{\infty+\mathrm{i}c} \int_{-\infty}^{\infty} A_0(\omega, k) \frac{\tilde{v}_0(Y, \omega, k)}{D(\omega, k)} \mathrm{e}^{\mathrm{i}[k(X-X_0)-\omega(T-T_0)]}\, \mathrm{d}\omega\, \mathrm{d}k, \tag{6.3}$$

where $A_0(\omega, k)$ is related to the Fourier–Laplace transform of the imposed distortion, $\tilde{v}_0(Y, \omega, k)$ satisfies the reduced Rayleigh equation corresponding to the nominally two-dimensional mean flow $U(\bar{t}, \bar{x}, Y, z)$ and $D(\omega, k) = 0$ is the corresponding dispersion relation. The k-integration is over the real axis and the ω-integration is over the Bramowitz contour, which can be continuously deformed onto the real axis when this local flow field is convectively unstable. The k-integration must then be deformed to lie below all the poles of the integrand that cross into the lower half-plane during this process. These poles correspond to the roots of the Rayleigh equation dispersion relation $D(\omega, k) = 0$ and the main contribution to the integrals in (6.3) will come from their residues when $X - X_0$ becomes large. $v_0(X, Y, T)$ is then given by

$$v_0(X, Y, T) = \int_{-\infty}^{\infty} A(\tilde{\omega}) \bar{v}_0(Y, \tilde{\omega}) \mathrm{e}^{\mathrm{i}[k(\tilde{\omega})(X-X_0)-\tilde{\omega}(T-T_0)]}\, \mathrm{d}\tilde{\omega}, \tag{6.4}$$

where $k(\tilde{\omega})$ denotes a root of the local dispersion relation and $\bar{v}_0(Y, \tilde{\omega})$ denotes the corresponding Rayleigh equation eigensolution for the nominally two-dimensional mean flow $U(\bar{t}, \bar{x}, Y, z)$. However, it is easy to show by direct substitution that $v_1(X, Y, T)$ grows linearly with X, T and, therefore, becomes $O(v_0(x, Y, t))$ when $X, T = O(\sigma/\bar{a}\delta\varepsilon)$, which means that the expansion breaks down when $\bar{t}, \bar{x} = O(1)$.

To obtain a global solution that is uniformly valid when the scaled variables $\bar{x}$ and $\bar{t}$ are $O(1)$ and reduces to the local solution (6.2) when the fast variables X and T are $O(1)$, we adopt the so-called slowly varying or WKBJ approach (Nayfeh 1973, p. 315 & ff) and substitute

$$v(X, Y, T; \bar{\varepsilon}) = \int_{-\infty}^{\infty} \bar{v}(Y : \bar{x}, \bar{t}; \tilde{\omega} : \bar{\varepsilon}) e^{i\, \Theta(\tilde{\omega}, \bar{x}, \bar{t})/\bar{\varepsilon}} \mathrm{d}\tilde{\omega}, \tag{6.5}$$

where

$$\bar{\varepsilon} \equiv \varepsilon\delta\, \bar{a}/\sigma, \tag{6.6}$$

and $\bar{v}(Y : \bar{x}, \bar{t}; \tilde{\omega} : \bar{\varepsilon})$ expands as

$$\bar{v}(Y : \bar{x}, \bar{t}; \tilde{\omega} : \bar{\varepsilon}) = \mathrm{A}(\bar{x}, \bar{t}; \tilde{\omega})\, \bar{v}_0(Y : \bar{x}, \bar{t}; \tilde{\omega}) + \bar{\varepsilon}\, \bar{v}_1(Y : \bar{x}, \bar{t}; \tilde{\omega}) + \cdots, \tag{6.7}$$

into the appropriately scaled linearized Navier–Stokes equations. $\bar{v}_0(Y : \bar{x}, \bar{t}; \tilde{\omega})$ will then satisfy the same reduced Rayleigh's equation as before if we put

$$k(\omega_0, \bar{x}, \bar{t}) \equiv \frac{\partial \Theta(\omega_0, \bar{x}, \bar{t})}{\partial \bar{x}}, \tag{6.8}$$

$$\omega(\omega_0, \bar{x}, \bar{t}) \equiv -\frac{\partial \Theta(\omega_0, \bar{x}, \bar{t})}{\partial \bar{t}}. \tag{6.9}$$

The 'slowly varying amplitude function' $A(\bar{x},\bar{t};\tilde{\omega})$ can be chosen to ensure solvability in the boundary-value problem for $\bar{v}_1(Y : \bar{x},\bar{t};\tilde{\omega})$, which means that the first-order term will no longer become large compared to the zeroth-order term when $\bar{x}, \bar{t} = O(1)$. (Nayfeh 1973, p. 315 & ff). We need not calculate this quantity here.

The zeroth-order dispersion relation $D(\omega, k, \bar{x},\bar{t}) = 0$ is determined by the same eigenvalue problem as the original local solution (6.2) and it, therefore, follows from (6.8) and (6.9) that the phase factor Θ satisfies the first-order partial differential equation

$$D\left(-\frac{\partial\Theta}{\partial\bar{t}},\ \frac{\partial\Theta}{\partial\bar{x}},\ \bar{x},\bar{t}\right) = 0, \tag{6.10}$$

whose complete integral can be written as (Garabedian 1964, p. 33)

$$\Theta = \vartheta(\bar{x},\bar{t};\omega_0, b_0), \tag{6.11}$$

where ω_0, b_0 are two independent parameters. The general solution can be obtained by eliminating ω_0 between

$$\Theta = \vartheta(\bar{x},\bar{t};\omega_0, b_0(\omega_0)) \tag{6.12}$$

and

$$\vartheta_{\omega_0}(\bar{\mathrm{x}},\bar{t};\omega_0, b_0(\omega_0)) + \vartheta_{b_0}(\bar{x},\bar{t};\omega_0, b_0(\omega_0))\frac{\mathrm{d}b_0(\omega_0)}{\mathrm{d}\omega_0} = 0, \tag{6.13}$$

where $b_0(\omega_0)$ is a given function and subscripts denote partial differentiation with respect to indicated arguments. Note that (6.13) determines ω_0 as a function of $\bar{\mathrm{x}},\bar{t}$. Equation (6.5) now becomes

$$v(X,Y,T;\bar{\varepsilon}) = \int_{-\infty}^{\infty} A(\bar{\mathrm{x}},\bar{t};\tilde{\omega})\bar{v}_0(Y : \bar{x},\bar{t};\tilde{\omega})\mathrm{e}^{\mathrm{i}\,\vartheta(\bar{\mathrm{x}},\,\bar{t};\tilde{\omega},\,b_0(\tilde{\omega}))/\bar{\varepsilon}}\mathrm{d}\tilde{\omega} \tag{6.14}$$

to the lowest order of approximation. Since $\vartheta(\bar{x},\bar{t};\tilde{\omega},\ b_0(\tilde{\omega}))/\bar{\varepsilon}$ will be large when $\bar{x},\bar{t} = O(1)$, we can use the method of steepest descent (Carrier, Krook & Pearson 1966, p. 272) to obtain

$$v(X,Y,T;\bar{\varepsilon}) \sim A(\bar{x},\bar{t})\left[\frac{2\pi\bar{\varepsilon}}{|\mathrm{d}^2\vartheta/\mathrm{d}\tilde{\omega}^2|_{\tilde{\omega}=\omega_0}}\right]^{1/2}\mathrm{e}^{\frac{\mathrm{i}}{\bar{\varepsilon}}\vartheta(\bar{x},\bar{t};\omega_0,\,b_0(\omega_0))\pm\mathrm{i}\,\pi/4}[\bar{v}_0(Y : \bar{x},\bar{t};\omega_0) + O(\bar{\varepsilon})], \tag{6.15}$$

where ± corresponds to $\mathrm{d}^2\vartheta/\mathrm{d}\tilde{\omega}^2 > / < 0$ and $\omega_0(\bar{\mathrm{x}},\bar{t})$ is determined from the solution of

$$\vartheta_{\omega_0}(\bar{\mathrm{x}},\bar{t};\omega_0, b_0(\omega_0)) + \vartheta_{b_0}(\bar{x},\bar{t};\ \omega_0, b_0(\omega_0))\frac{\mathrm{d}b_0(\omega_0)}{\mathrm{d}\omega_0} = 0, \tag{6.16}$$

which is formally the same as (6.13) and, therefore, implies that $\vartheta(\bar{x},\bar{t};\omega_0,\ b_0(\omega_0))$ is a general solution of the dispersion equation (6.10), which means that (6.15) is also a local solution to the original Rayleigh equation.

6.2. *Initial-value problem for dispersion equation solution* $\vartheta(\bar{x},\ \bar{t};\ \tilde{\omega},\ b_0(\tilde{\omega}))$

In order to insure that the global solution (6.14) reduces to the local solution (6.4) at $\bar{\mathrm{x}},\bar{t} = \bar{\mathrm{x}}_0, \bar{t}_0 \equiv \bar{\varepsilon}x_0, \bar{\varepsilon}t_0$, it is necessary that

$$\frac{1}{\bar{\varepsilon}}\left[\vartheta(0,\ 0;\ \tilde{\omega},\ b_0(\tilde{\omega})) + \left(\frac{\partial\vartheta}{\partial\bar{t}}\right)_{\bar{x}_0,\bar{t}_0}(\bar{t}-\bar{t}_0) + \left(\frac{\partial\vartheta}{\partial\bar{x}}\right)_{\bar{x}_0,\bar{t}_0}(\bar{x}-\bar{x}_0)\right]$$
$$\rightarrow k\,(\tilde{\omega})\,(x-x_0) - \tilde{\omega}\,(t-t_0)\ \text{ as } \bar{x},\bar{t}\rightarrow\bar{x}_0,\bar{t}_0, \tag{6.17}$$

which implies that

$$\vartheta(\bar{x},\bar{t};\tilde{\omega},\, b_0(\tilde{\omega}))=0,\ \frac{\partial\vartheta}{\partial\bar{t}}=-\tilde{\omega}\quad \text{at}\quad \bar{x},\bar{t}=\bar{x}_0,\bar{t}_0. \tag{6.18}$$

Alternatively, the dispersion relation $D(\omega,k,\bar{x},\bar{t})=0$ can be solved for k to obtain $k=K\,(\omega,\bar{x},\bar{t})$,which can be used to replace the second condition in (6.18) by

$$\frac{\partial\vartheta}{\partial\bar{x}}=K(\tilde{\omega},\bar{x},\bar{t}\,)\quad \text{at}\quad \bar{x},\bar{t}=\bar{x}_0,\bar{t}_0. \tag{6.19}$$

The solution to the initial-value problem (6.10), (6.12) and (6.18) can then be found by solving

$$D\left(-\frac{\partial\vartheta}{\partial\bar{t}},\ \frac{\partial\vartheta}{\partial\bar{\mathrm{x}}},\ \bar{x},\bar{t}\right)=0\quad \text{for}\quad \bar{x}_1<\bar{x}<\bar{x}_2,\ \bar{t}>\bar{t}_0, \tag{6.20}$$

subject to the initial condition

$$\vartheta=\vartheta_0(\bar{x})\equiv\vartheta(\bar{x},\bar{t}_0)\quad \text{for}\ \bar{t}=\bar{t}_0, \tag{6.21}$$

where $\vartheta_0(\bar{x})$ satisfies the ordinary differential equation

$$\frac{\mathrm{d}\vartheta_0}{\mathrm{d}\bar{x}}=K(\tilde{\omega},\bar{x},\bar{t}_0),\quad \text{for}\quad \bar{x}_1<\bar{x}<\bar{x}_2, \tag{6.22}$$

subject to the initial condition

$$\vartheta_0(\bar{x})=0\quad \text{at}\quad \bar{x}=\bar{x}_0. \tag{6.23}$$

The steepest descent point $\omega_0(\bar{x},\bar{t}\,)$ will in general be complex, with the phase factor $\vartheta(\bar{x},\ \bar{t};\ \omega_0,\ b_0(\omega_0))$ being an analytic continuation of $\vartheta(\bar{x},\ \bar{t};\ \tilde{\omega},\ b_0(\tilde{\omega}))$ into the complex $\tilde{\omega}$-plane along the steepest descent path. This implies that $\vartheta(\bar{x},\ \bar{t};\ \tilde{\omega},\ b_0(\tilde{\omega}))$ can be found by analytically continuing the initial-value problem (6.20)–(6.23) into the complex plane. In other words, $\vartheta(\bar{x},\bar{t};\ \omega_0,\ b_0(\omega_0))$ can be found by solving the initial-value problem (6.20)–(6.23) for complex $\tilde{\omega}=\omega_0(\bar{x},\ \bar{t})$.

6.3. *Numerical solution of dispersion equation*

As noted in §6.1, the numerical computation of the wave-packet phase factor $\vartheta(\bar{x},\ \bar{t};\ \omega_0(\bar{x},\ \bar{t}),\ b_0(\omega_0(\bar{x},\ \bar{t})))$ is based on the numerical dispersion relation (or NDR) obtained from the local Rayleigh equation eigensolutions. The NDR can be calculated either by finding the complex frequency $\omega=\varOmega\ (k,\bar{x},\ \bar{t})$ as a function of complex wavenumber (corresponding to temporal stability analysis) or by finding the wavenumber $k=K(\omega,\ \bar{x},\ \bar{t})$, as a function of complex frequency (corresponding to spatial stability analysis) – both of which lead to identical conclusions about the linear instability of the local flow, but their numerical implementation can be very different (Suslov 2006). The first leads to a linear eigenvalue problem for the frequency which we solved either as a matrix eigenvalue problem or by using a shooting method. The second leads to a nonlinear eigenvalue problem that we could only solve by using a shooting method – which usually requires a reasonably accurate initial guess in order to converge. The temporal stability analysis was, therefore, preferred when investigating the convective/absolute instability boundary. This was done by using Kupfer's cusp map method (Kupfer, Bers & Ram 1987), which involves mapping a section of the k-plane (for example, lines parallel to the real k-axis situated in the lower half-plane with progressively decreasing imaginary part) into the ω-plane (Agarwal &

Morris 2006). The NDR was calculated at discrete points within the spatio-temporal domain $[\bar{x}_1, \bar{x}_2] \times [\bar{t}_0, \bar{t}]$. Instability occurs when any part of the $\omega(k)$ map lies in the upper-half ω-plane, which turned out to be the case whenever the streamwise velocity profiles were inflectional. No cusp point was encountered anywhere in the upper-half ω-plane – which means that the instability was always convective.

The monochromatic wave phase factor $\vartheta(\bar{x}, \bar{t}; \tilde{\omega}, b_0(\tilde{\omega}))$ was found by solving (6.20) rewritten as

$$\frac{\partial \vartheta_0}{\partial \bar{t}} = -\Omega\left(\frac{\partial \vartheta_0}{\partial \bar{x}}, \bar{x}, \bar{t}\right) \tag{6.24}$$

which was then discretized as

$$\vartheta_0(\bar{x}, \bar{t} + \Delta\bar{t}) = \vartheta_0(\bar{x}, \bar{t}) - \Delta\bar{t} \cdot \Omega\left(\frac{\vartheta_0(\bar{x} + \Delta\bar{x}) - \vartheta_0(\bar{x})}{\Delta\bar{x}}, \bar{x}, \bar{t}\right), \tag{6.25}$$

subject to the initial condition (6.21), where ϑ_0 is determined by the ordinary differential equation (6.22) which was discretized as

$$\vartheta_0(\bar{x} + \Delta\bar{x}) = \vartheta_0(\bar{x}) + \Delta\bar{x} \cdot K(\tilde{\omega}, \bar{x}, \bar{t}_0) \qquad \text{for} \quad \bar{x}_1 < \bar{x} < \bar{x}_2. \tag{6.26}$$

The solution of this problem requires that the NDR be determined both as $\omega = \Omega\,(k, \bar{x}, \bar{t})$ and as $k = K(\omega, \bar{x}, \bar{t})$. These relations were calculated at discrete points in the $[\bar{x}_1, \bar{x}_2] \times [\bar{t}_0, \bar{t}]$ domain and interpolated by putting splines through the data to transform the NDRs into continuous smooth bivariate functions. The local wave-packet frequency $\omega_0(\bar{x}, \bar{t})$ and phase factor $\vartheta(\bar{x}, \bar{t}; \omega_0(\bar{x}, \bar{t}), b_0(\omega_0(\bar{x}, \bar{t})))$ were then found by iterating on $\tilde{\omega}$ until a saddle point of $\vartheta(\bar{x}, \bar{t}; \tilde{\omega}, b_0(\tilde{\omega}))$ was found at the point $\bar{x}$, $\bar{t}$. The initial guess for the first $\bar{x}$, $\bar{t}$ step was obtained from the local (uniform medium) stationary phase condition

$$\frac{\partial K(\tilde{\omega}, \bar{x}_0, \bar{t}_0)}{\partial \tilde{\omega}} = \frac{\bar{t} - \bar{t}_0}{\bar{x} - \bar{x}_0}, \tag{6.27}$$

and the local wave packet frequency $\omega_0(\bar{x}, \bar{t})$ from the previous step was used as the initial guess for each succeeding step.

As implied by the discrete forms (6.25) and (6.26), equations (6.22) and (6.24) were both solved using first-order finite-difference schemes on a relatively coarse grid owing to the large amount of data to be stored. We quantified the error introduced by the numerical method used to solve the equations (6.25) and (6.26) by varying of the spatial step size (or the number of grid points) and found no significant variation in the calculated phase factor. The error analysis described in § 5 (see (5.10) and (5.11)) was repeated here with an error bound of $\varepsilon^* \cong 5 \times 10^{-3}$.

7. Results and discussion

The vorticity of the imposed upstream distortion (2.2) is nearly perpendicular to the plate. Its vortex lines are convected downstream by the predominantly inviscid flow and become elongated as they pass over the plate – leading to infinite velocities and infinitesimal length scales which must be eliminated by viscous effects. As in GLC, this vortex stretching produces the usual logarithmic singularity in the initial inviscid solution (Hunt & Carruthers 1990) and a much more interesting nonlinear singularity – which generates small spanwise length scales in the approaching boundary layer – further downsteam in the flow. The focus of this paper is on this latter three-dimensional unsteady boundary-layer region, in which the small spanwise length scales give rise to elongated streamwise streaks.

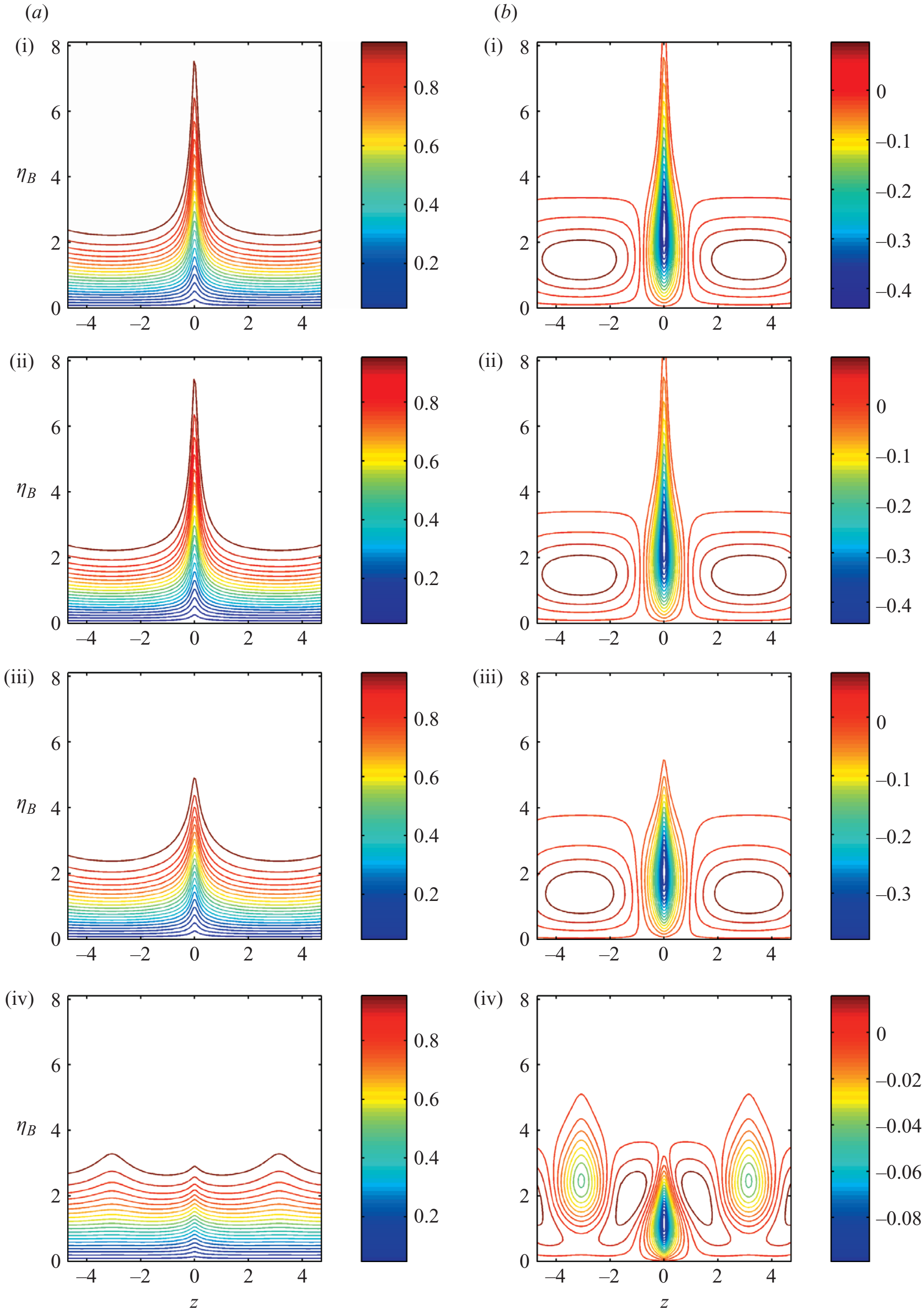

FIGURE 1(a,b). For caption see facing page.

As noted in § 5, the boundary-layer flow depends on the imposed upstream distortion only through the function $g\,(\bar{\tau}, z)$ defined by (2.18), (2.32) and (3.10). For the sake of simplicity, we focus on upstream distortions that are periodic in both the scaled time $\bar{t}$ and the spanwise coordinate z. The numerical solutions described in § 5 are based

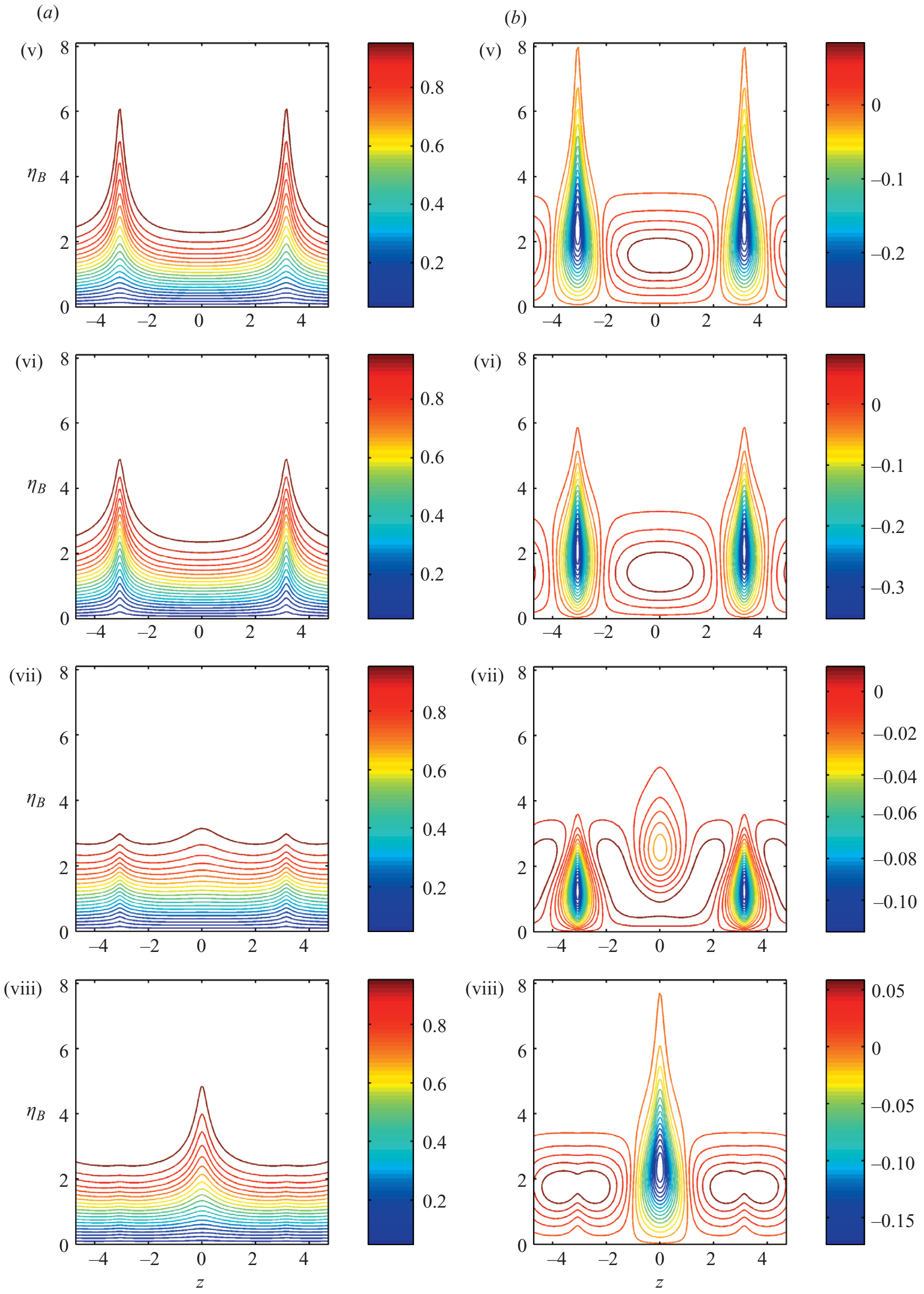

FIGURE 1. Contours of (*a*) the disturbed streamwise velocity and (*b*) the difference between the disturbed streamwise velocity and the Blasius streamwise velocity with (i) $\bar{t} = 0$, (ii) 0.3, (iii) 0.6, (iv) 0.9, (v) 1.2, (vi) 1.5, (vii) 1.8, (viii) 2.

on solving an initial-value problem with the initial condition being the steady flow produced by the steady upstream distortion $g\,(-\bar{x}, z)$. We also solved the steady-flow problem corresponding to the upstream distortion $g\,(0, z)$ for many different choices of this function and, as in GLC, found that the boundary-layer velocity profiles were always non-inflectional everywhere upstream of the downstream singularity – which means that they can only support slowly growing viscous instabilities. However, the unsteady calculations show that the instantaneous velocity profiles can become highly inflectional when the upstream flow is allowed to oscillate on the slow time scale $\bar{t} = \varepsilon \bar{a} t/\sigma$. The local profiles (at any given point in the boundary layer) are only inflectional during part of the oscillation cycle, but, during that time, they can support rapidly growing inviscid (i.e. Rayleigh) instabilities, which evolve on much faster time and (streamwise) space scales than the slow time and (streamwise) space scales $\bar{t}$ and $\bar{x}$ on which the boundary layer develops. So, as first noted by Cowley (1985) and subsequently by Wu (1992) and Wu, Lee & Cowley (1993) (see also Wu & Choudhari, 2003), these disturbances can rapidly grow to nonlinear amplitudes and break down into turbulent spots before the cycle reverses and the inflection points disappear. Wu & Choudhari (2003) considered long-wavelength disturbances, which grow more slowly than those considered in this paper; but these disturbances can begin to grow even when the induced mean flow changes are very small, i.e. $o\,(1)$.

Since the boundary layer behaves like a locally parallel flow, the induced disturbances are locally determined by the Rayleigh equation, but evolve like slowly modulated wave packets on the longer length and time scales of the unsteady boundary-layer flow. The relevant wave-packet solution can be constructed from the local Rayleigh equation dispersion relation, as was done in § 6.

To fix ideas, all computations were carried out with the simple upstream distortion

$$u_\infty = -[\sin \bar{k}(\bar{t} - \bar{x})] \cos z. \tag{7.1}$$

More complicated distortions will obviously produce more complicated results. Equations (3.10), (5.1)–(5.9) and (7.1) show that the unsteady boundary flow will then depend on the single parameter $\bar{k}$, which, for definiteness, we now set equal to 5. Figure 1(*a*) is a plot of the contours of constant streamwise velocity in a cross-flow plane at the typical streamwise location of $\bar{x} = 0.7$ for different values of the scaled time variable $\bar{t}$. They clearly show that there is a thickening and thinning of the boundary layer that gradually moves back and forth across the flow. It was implicitly noted in § 4.1 that the undisturbed boundary-layer solution would correspond to the Blasius result

$$U \equiv U_B = F'(\eta_B), \tag{7.2}$$

where η_B is the Blasius variable (4.4) and $F'(\eta_B)$ is the Blasius function determined by (4.5) to (4.7). So contours of constant $U - U_B$ characterize the streamwise velocity excess/deficit relative to the undisturbed flow. Negative $U - U_B$ regions correspond to the low-speed streaks that are frequently observed in experiments. The contours are plotted in figure 1(*b*) for the same conditions as the U contours. They show, among other things, that the streaks move across the boundary layer and that any given point in the boundary layer will lie on a streak during part of the oscillation cycle and in a relatively undisturbed region during the rest of the cycle. This can be seen more clearly from the $U - U_B$ profiles ploted in figure 2 for the same time intervals.

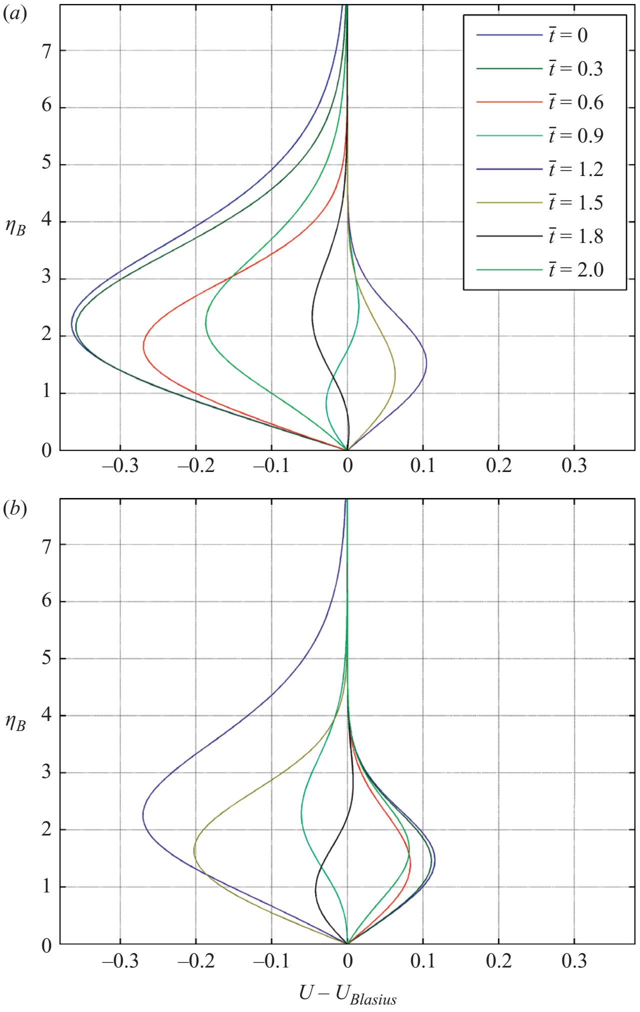

FIGURE 2. Difference between the instantaneous streamwise velocity and Blasius velocity at (*a*) $z = 0$ and (*b*) $z = \pi$ for different times (corresponding to those in figure 1), as a function of cross-stream Blasius variable, η_B.

Figure 3 is a plot of the corresponding $U'' \equiv \partial^2 U/\partial \eta_B^2$ profiles. They clearly show that, although the most highly inflectional regions tend to lie on the low-speed streaks, the boundary layer can remain inflectional even after the streaks have moved to a new location in the layer – which means that disturbances can continue to grow even after the low-speed streaks have passed. While inflectional profiles do not automatically guarantee instability, it appears that they do in the present case. Some typical temporal growth rate curves are shown at a few selected time intervals in figure 4. They suggest that the most highly inflectional profiles produce the most rapid growth. The present results show that the $U - U_B$ profiles and contours depend on the upstream distortion amplitude ε and leading-edge bluntness parameter $\bar{a}$ only through the scaled variables $\bar{x}$ and $\bar{t}$, which means that these quantities can affect these profiles and contours only by changing the time and streamwise location at which they occur. This may, at least

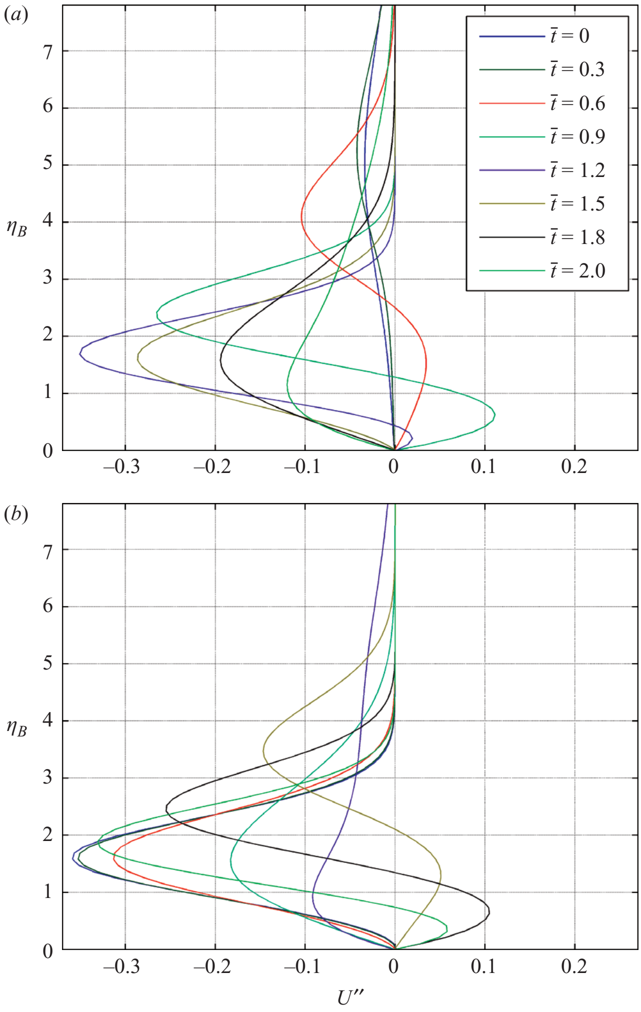

FIGURE 3. Second derivative of the streamwise velocity with respect to η_B at (*a*) $z = 0$ and (*b*) $z = \pi$, as a function of cross-stream Blasius variable, η_B for different times (corresponding to those in figure 1).

in part, explain why Kendall (1991) and Watmuff (1997) were unable to detect any leading-edge effect on the Klebanoff modes.

The most important results are the two-dimensional wave-packet solutions developed in § 6. Their phase surfaces $\vartheta(\bar{x}, \bar{t}; \omega_0(\bar{x}, \bar{t}), b_0(\omega_0(\bar{x}, \bar{t})))$ move along the trajectories $\bar{x}_{wp} = \bar{x}_{wp}(\bar{t})$, described in Appendix B and, while the wave packets in the NFL simulation are clearly three-dimensional, we feel that the relevant physics can best be illustrated by considering the much simpler two-dimensional case. Figures 5(*a*) and 6(*a*) show the growth, $-\mathrm{Im}\vartheta$, of two typical wave packets along these trajectories. The actual wave-packet trajectories $\bar{x}_{wp} = \bar{x}_{wp}(\bar{t})$, are shown in figures 5(*b*) and 6(*b*). The slopes $\mathrm{d}\bar{x}_{wp}/\mathrm{d}\bar{t}$ of these curves are the wave-packet phase velocities normalized by the upstream velocity U_∞. A typical value for these quantities is ≈ 0.2, which – considering the two-dimensional nature of the present result – is remarkably close to the value of 0.5 given in NFL.

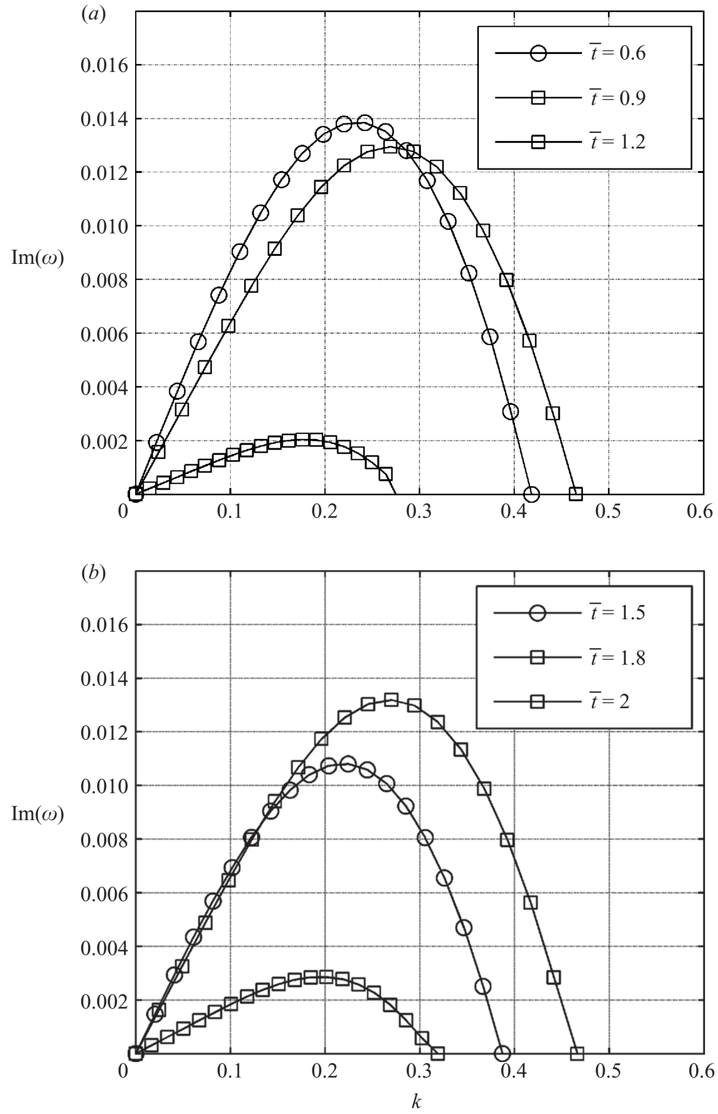

FIGURE 4. Selected temporal growth rates corresponding to the inflectional profiles in figure 3. (*a*) $z = 0$, (*b*) $z = \pi$.

The corresponding $U - U_B$ and U'' profiles are shown at selected points along these trajectories in figures 5(*c, d*) and 6(*c, d*). Figures 5(*e*) and 6(*e*) show contours of constant streamwise velocity in the cross-flow planes at various points along the trajectories. Although the phenomenon under consideration is expected to occur at fairly high free-steam turbulence intensities, $O(0.05)$ or so, the figures show that the overall wave-packet growth exp $(\mathrm{Im}\vartheta/\bar{\varepsilon})$, which depends on the additional parameter $\bar{\varepsilon} \equiv \varepsilon\,\bar{a}\delta/\sigma = \sqrt{\varepsilon\,\bar{a}\delta/R_\lambda\sigma}$ (see (4.11)), will be rather small unless $\bar{\varepsilon}$ is also relatively small, which it is in the NFL simulation since $\delta \sim 0.06$, $\varepsilon\,\delta$ is then about 3×10^{-3} and the maximum value of $\mathrm{Im}\vartheta/\bar{\varepsilon}$ is, therefore, about 30.

Notice that $\exp(\mathrm{Im}\vartheta/\bar{\varepsilon})$ will be large when the product $\varepsilon\,\bar{a}$ of the upstream distortion amplitude and the leading-edge bluntness is small. The wave packets

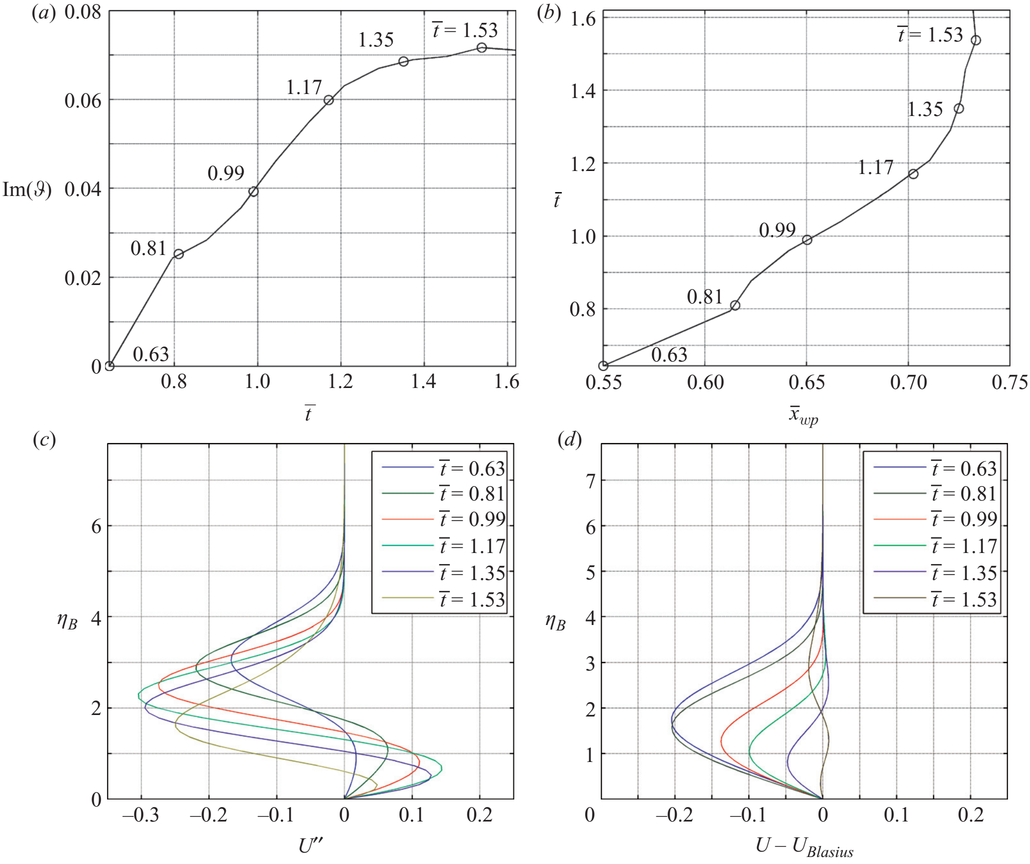

FIGURE 5(a–d). For caption see page 120.

are, therefore, likely to reach large amplitudes and become nonlinear while the local velocity profiles are still streak-like for thin plates and/or low free-stream turbulence levels. They are unlikely to reach such amplitudes until the low-speed streaks have moved to a new location when the plate is sufficiently thick and/or the free-stream turbulence levels are sufficiently high. This could explain why the spot precursor wave packet appear to grow on the turbulent streaks in the NFL simulations when either or both of these quantities are small and reach detectable amplitudes only after the streak has moved to a new location and, therefore, appear to grow on the relatively undisturbed region between the streaks when they are large. Figures 5(f) and 6(f) show the wave-packet mode shapes at selected points along the wave-packet trajectory. These results indicate that the wave packet will be largely confined to the lower part of the boundary layer by the time it reaches its maximum amplitude – which is again consistent with the NFL observations.

Although the dimensionality of the wave packet is expected to have only a quantitative effect on the initial linear stage, it is likely to have an important qualitative effect in the final nonlinear stage, as suggested by the work of Wu *et al.* (1993) who used a similar framework to analyse the disturbance growth in oscillating Stokes layers. By considering a pair of interacting oblique modes, they showed that strong nonlinear critical-layer effects eventually come into play at very small amplitudes for such three-dimensional modes and ultimately cause the disturbance to exhibit explosive growth – which they associate with the breakdown into turbulence. Wu &

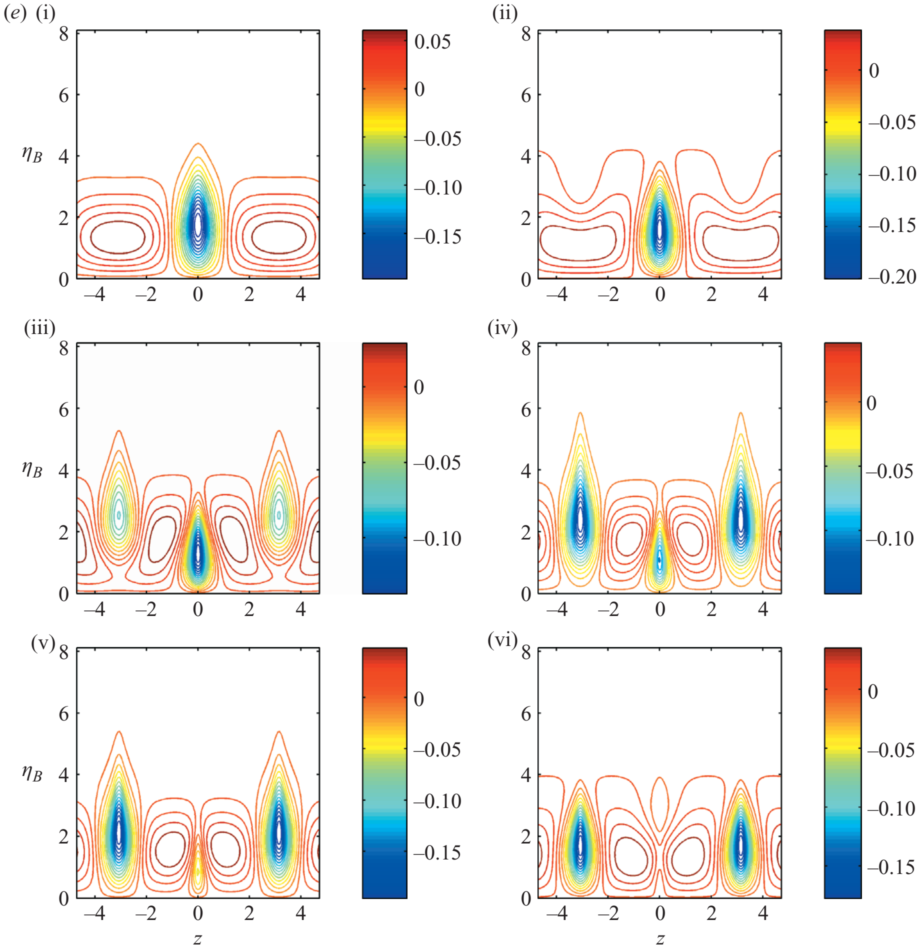

FIGURE 5(*e*). For caption see page 120.

Choudhari (2003) considered the nonlinear evolution of secondary instabilities in a similar fashion.

The authors would like to thank Dr Abdollah A. Afjeh, Professor and Chairman of the MIME Department, University of Toledo, for his inspiring and encouraging support, Dr Ray Hixon, Associate Professor at the MIME Department, for his helpful comments regarding the numerical implementation and Dr Stewart Leib of the Ohio Aerospace Institute for his helpful comments on the manuscript. Funding for this work by NASA's subsonic sixed wing project is gratefully acknowledged

Appendix A

Re-expanding (2.21) and (2.14) shows that

$$\nabla^2\tilde{\phi}_0 \to -\frac{\partial}{\partial y}u_\infty(\bar{x}-\bar{t},\boldsymbol{x}_\perp)\Delta'_+(y) - \frac{\varepsilon}{\sigma}\bar{a}\left[\frac{\partial}{\partial \bar{x}}u_\infty(\bar{x}-\bar{t},\boldsymbol{x}_\perp)\Delta'_+(y)\Delta_+(y)+\bar{v}_\infty\left(\bar{x}-\bar{t}+\frac{\varepsilon}{\sigma}\Delta_+,\boldsymbol{x}_\perp\right)\right]+\cdots \quad \text{as } x \to \infty \tag{A 1}$$

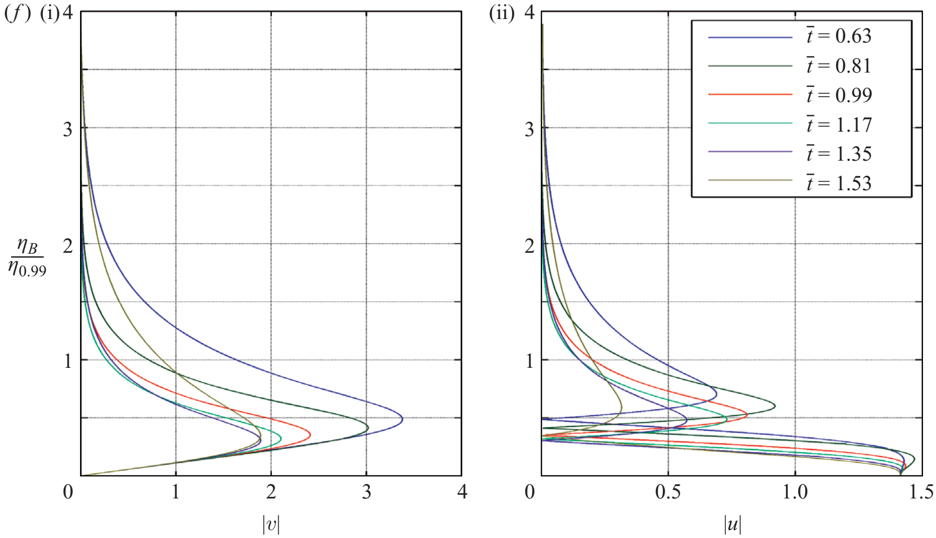

FIGURE 5. Two-dimensional wave-packet solution initiated at $z=0$, $\bar{t}_0=0.63$, $\bar{x}_0=0.55$. (*a*) Total wave-packet growth. (*b*) Wave-packet trajectory. (*c*) Second derivative of the streamwise velocity with respect to η_B, at $z=0$ as a function of cross-stream Blasius variable, η_B for different times corresponding to those in (*a*). (*d*) Difference between the instantaneous streamwise velocity and Blasius velocity at $z=0$ for different times (corresponding to those in (*a*)), as a function of cross-stream Blasius variable, η_B. (*e*) Contour of the difference between the disturbed streamwise velocity and the Blasius streamwise velocity for (i) $\bar{t}=0.63$, (ii) 0.81, (iii) 0.99, (iv) 1.17, (v) 1.35, (vi) 1.53, corresponding to those in (*a*). (*f*) Wave-packet mode shapes, (i) normal velocity fluctuation, (ii) streamwise velocity fluctuation at various points along the trajectory, corresponding to those indicated in (*b*).

and

$$\tilde{\boldsymbol{u}}^{\boldsymbol{I}} \to \hat{\boldsymbol{i}}\, u_\infty(\bar{x}-\bar{t}, \boldsymbol{x}_\perp) + \hat{\boldsymbol{j}}\, u_\infty(\bar{x}-\bar{t}, \boldsymbol{x}_\perp)\Delta'_+(y) \\ + \frac{\varepsilon}{\sigma}\bar{a}\left[\hat{\boldsymbol{i}}\, \frac{\partial}{\partial \bar{x}} u_\infty(\bar{x}-\bar{t}, \boldsymbol{x}_\perp)\Delta_+ + \hat{\boldsymbol{j}}\, \bar{v}_\infty(\bar{x}-\bar{t}, \boldsymbol{x}_\perp) + \hat{\boldsymbol{k}}\, \bar{w}_\infty(\bar{x}-\bar{t}, \boldsymbol{x}_\perp)\right] + \cdots \tag{A 2}$$

as $x \to \infty$, where $\hat{\boldsymbol{i}}$ and $\hat{\boldsymbol{j}}$ denote unit vectors in the x- and y-directions. It now follows from (2.22) that

$$\frac{\partial}{\partial y}\left(\tilde{\phi} + \frac{\varepsilon}{\sigma}\bar{a}\,\tilde{\phi}_1\right) = \frac{\partial \tilde{\phi}_0}{\partial y} + u_\infty(\bar{x}-\bar{t}, \boldsymbol{x}_\perp)\,\Delta'_+(y), \tag{A 3}$$

$$\frac{\partial^2}{\partial y^2}\left(\tilde{\phi} + \frac{\varepsilon}{\sigma}\bar{a}\,\tilde{\phi}_1\right) = \frac{\partial^2 \tilde{\phi}_0}{\partial y^2} + \frac{\partial}{\partial y} u_\infty(\bar{x}-\bar{t}, \boldsymbol{x}_\perp)\,\Delta'_+(y), \tag{A 4}$$

which, in view of (A 1), shows that

$$\nabla^2\left(\tilde{\phi} + \frac{\varepsilon}{\sigma}\bar{a}\,\tilde{\phi}_1\right) \to \left(\frac{\partial^2}{\partial z^2} + \frac{\partial^2}{\partial x^2}\right)\int u_\infty(\bar{x}-\bar{t}, \boldsymbol{x}_\perp)\,\Delta'_+(y)\,\mathrm{d}y \\ - \frac{\varepsilon}{\sigma}\bar{a}\left[\frac{\partial}{\partial \bar{x}} u_\infty(\bar{x}-\bar{t}, \boldsymbol{x}_\perp)\,\Delta'_+(y)\,\Delta_+(y) + \bar{v}_\infty\left(\bar{x}-\bar{t}+\frac{\varepsilon}{\sigma}\Delta_+, \boldsymbol{x}_\perp\right)\right] + \cdots$$

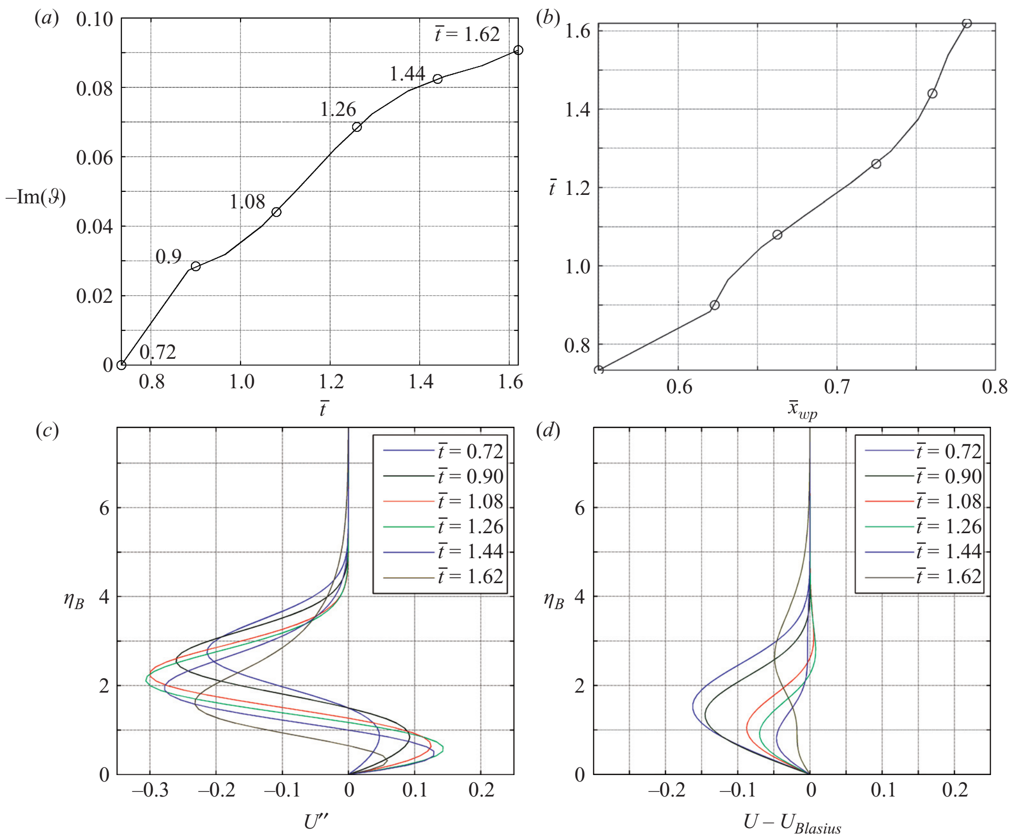

FIGURE 6(*a–d*). For caption see page 123.

$$
\begin{aligned}
&\rightarrow \frac{\partial^2}{\partial z^2} \int u_\infty\,(\bar{x}-\bar{t},\,\boldsymbol{x}_\perp)\,\Delta'_+(y)\,\mathrm{d}y \\
&\quad -\frac{\varepsilon}{\sigma}\bar{a}\left[\frac{\partial}{\partial \bar{x}}u_\infty(\bar{x}-\bar{t},\,\boldsymbol{x}_\perp)\Delta'_+(y)\Delta_+\,(y)+\bar{v}_\infty\left(\bar{x}-\bar{t}+\frac{\varepsilon}{\sigma}\bar{a}\Delta_+,\,\boldsymbol{x}_\perp\right)\right]+\cdots \qquad \text{(A 5)}
\end{aligned}
$$

On the other hand, (2.10) (2.22) and (A 2) imply that

$$
\begin{aligned}
\tilde{\boldsymbol{u}}_0 \rightarrow\ &\hat{\boldsymbol{i}}\,u_\infty(\bar{x}-\bar{t},\,\boldsymbol{x}_\perp)+\nabla\left(\tilde{\phi}+\frac{\varepsilon}{\sigma}\bar{a}\tilde{\phi}_1\right)-\hat{\boldsymbol{k}}\int \frac{\partial}{\partial z}u_\infty\,(\bar{x}-\bar{t},\,\boldsymbol{x}_\perp)\,\Delta'_+(y)\,\mathrm{d}y \\
&+\frac{\varepsilon}{\sigma}\bar{a}\left[\hat{\boldsymbol{i}}\frac{\partial}{\partial \bar{x}}\,(u_\infty(\bar{x}-\bar{t},\,\boldsymbol{x}_\perp)\Delta_+-\int u_\infty(\bar{x}-\bar{t},\,\boldsymbol{x}_\perp)\Delta'_+(y)\,\mathrm{d}y)\right. \\
&\left.+\hat{\boldsymbol{j}}\,\bar{v}_\infty\,(\bar{x}-\bar{t},\,\boldsymbol{x}_\perp)+\hat{\boldsymbol{k}}\,\bar{w}_\infty(\bar{x}-\bar{t},\,\boldsymbol{x}_\perp)\right]+\cdots.
\end{aligned}
$$

$$
\begin{aligned}
&=\hat{i}\,u_\infty\,(\bar{x}-\bar{t},\,x_\perp)+\nabla\left(\tilde{\phi}+\frac{\varepsilon}{\sigma}\bar{a}\tilde{\phi}_1\right)-\hat{k}\frac{\partial}{\partial z}\int u_\infty\,(\bar{x}-\bar{t},\,x_\perp)\,\Delta'_+\,(y)\,\mathrm{d}y \\
&\quad+\frac{\varepsilon}{\sigma}\bar{a}\left[\hat{i}\frac{\partial}{\partial \bar{x}}\int \nabla_+(y)\frac{\partial}{\partial y}u_\infty(\bar{x}-\bar{t},\,\boldsymbol{x}_\perp)\,\mathrm{d}y+\hat{\boldsymbol{j}}\bar{v}_\infty(\bar{x}-\bar{t},\,\boldsymbol{x}_\perp)+\hat{k}\,\bar{w}_\infty\,(\bar{x}-\bar{t},\,x_\perp)\right]+\cdots. \\
&\hspace{30em}\text{(A 6)}
\end{aligned}
$$

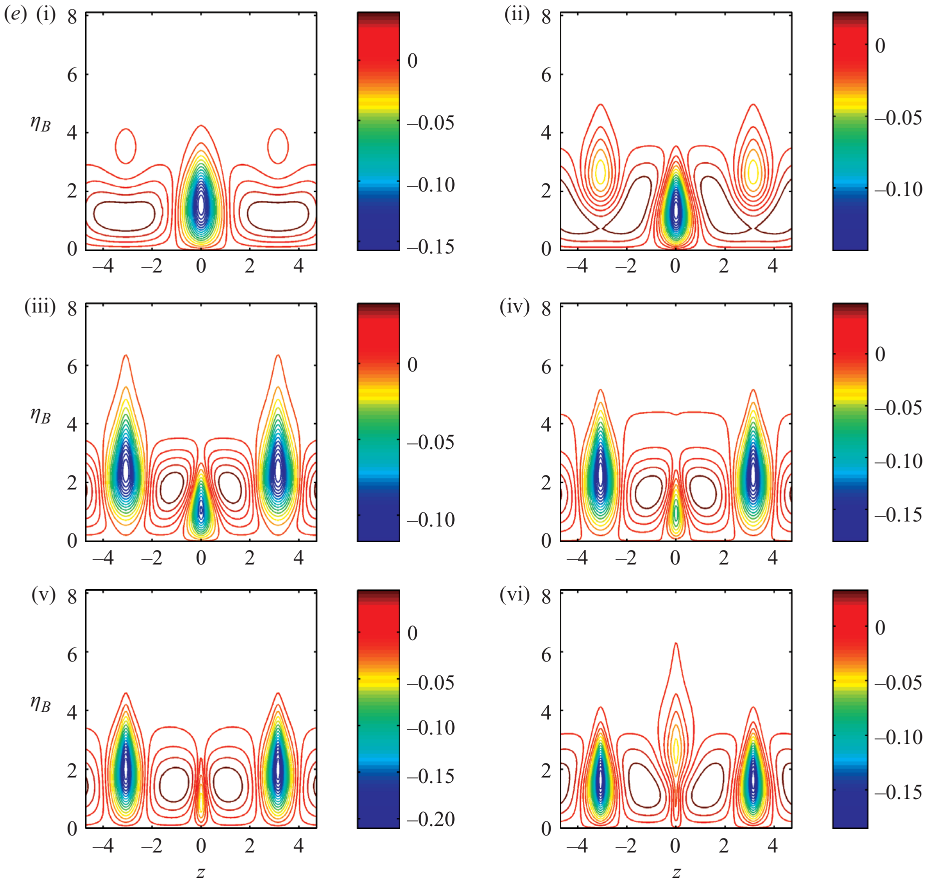

FIGURE 6(e). For caption see page 123.

as $x \to \infty$. It now follows from (2.22) and (2.23) that $\tilde{\phi}$ is independent of x and that (2.24) and (2.25) apply.

Appendix B

Since the wave packets are only slowly modulated and have relatively modest growth rates, they will appear to propagate along the curves, say $x_{wp} = \bar{x}_{wp}(\bar{t})$, in the $(\bar{x},\, \bar{t}\,)$-plane on which the real part of their phase remains constant and are, therefore determined by

$$Re\frac{\mathrm{d}\vartheta}{\mathrm{d}\bar{t}} = \left(Re\frac{\partial\vartheta}{\partial\bar{x}}\right)\frac{\mathrm{d}\bar{x}_{wp}}{\mathrm{d}\bar{t}} + Re\frac{\partial\vartheta}{\partial\bar{t}} = 0,$$

or

$$\frac{\mathrm{d}\bar{x}_{wp}}{\mathrm{d}\bar{t}} = H(\bar{x}_{wp}, \bar{t}\,), \tag{B 1}$$

where

$$H(\bar{x}, \bar{t}) \equiv -\frac{Re(\partial\vartheta(\bar{x}, \bar{t})/\partial\bar{t})}{Re(\partial\vartheta(\bar{x}, \bar{t})/\partial\bar{x})},$$

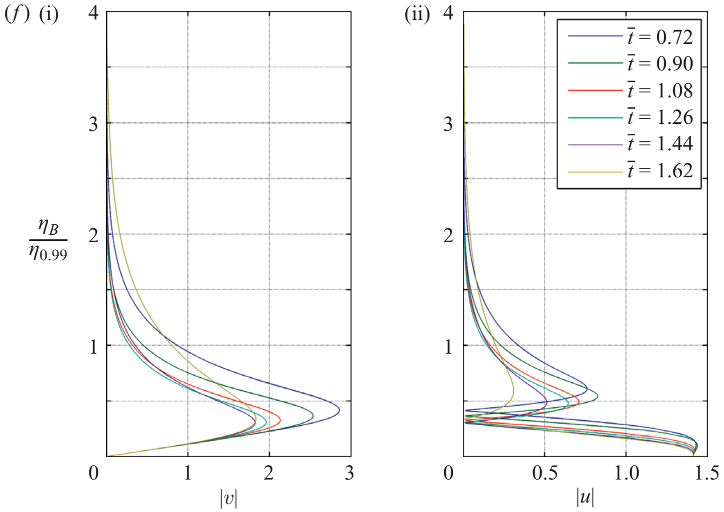

FIGURE 6. Two-dimensional wave-packet solution initiated at $z=0$, $\bar{t}_0=0.72$, $\bar{x}_0=0.55$. (*a*) Total wave-packet growth. (*b*) Wave-packet trajectory. (*c*) Second derivative of the streamwise velocity with respect to η_B, at $z=0$ as a function of cross-stream Blasius variable, η_B for different times corresponding to those in (*a*). (*d*) Difference between the instantaneous streamwise velocity and Blasius velocity at $z=0$ for different times corresponding to those in (*a*) as a function of cross-stream Blasius variable, η_B. (*e*) Contours of the difference between the disturbed streamwise velocity and the Blasius streamwise velocity for (i) $\bar{t}=0.72$, (ii) 0.9, (iii) 1.08, (iv) 1.26, (v) 1.44, (vi) 1.62, corresponding to those in (*a*). (*f*) Wave-packet mode shapes, (i) normal velocity fluctuation, (ii) streamwise velocity fluctuation at various points along the trajectory, corresponding to those indicated in (*b*).

The wave-packet trajectories in the $(\bar{x}, \bar{t})$-plane can therefore be found by solving the first-order nonlinear partial differential equation (B 1) subject to the initial condition

$$\bar{x}_{wp}(\bar{t}_0) = \bar{x}_0. \tag{B 2}$$

REFERENCES

AGARWAL, A. & MORRIS, P. J. 2006 Numerical computation of the linear convective and absolute stability of free-shear flow. *Computers Fluids* **35**, 1282–1289.

CARRIER, G. F., KROOK, M. & PEARSON, C. E. 1966 *Functions of a Complex Variable*. McGraw–Hill.

CEBECI, T., KHATTAB, A. K. & STEWARTSON, K. 1981 Three-dimensional laminar boundary layers and the ok of accessibility. *J. Fluid Mech.* **107**, 57–87.

CEBECI, T. & SMITH, A. M. O. 1974 *Analysis of Turbulent Boundary Layers*. Academic.

COWLEY, S. J. 1985 *High Frequency Rayleigh Instability of Stoked Layers, Stability of Time Dependent and Spatially Varying Flows* (ed. D. L. Dwoyer & M. I. Hussaini). Springer.

CROW, S. C. 1966 The spanwise perturbation of two-dimensional boundary layers. *J. Fluid Mech.* **24**, 153–164.

DARWIN, C. 1954 A note on hydrodynamics. *Proc. Camb. Phil. Soc.* **49**, 342–354.

GAITONDE, A. L. 1998 A Dual-time method for two-dimensional unsteady incompressible flow calculation. *Intl J. Number Meth. Engng* **41**, 1153–1166.

GARABEDIAN, P. R. 1964 *Partial Differential Equations*. John Wiley.

GOLDSTEIN, M. E. 1978 Unsteady vortical and entropic distortions of potential flows round arbitrary obstacles. *J. Fluid Mech.* **89**, 433–468.

GOLDSTEIN, M. E. 1979 Turbulence generated by the interaction of entropy fluctuations with non-uniform mean flows. *J. Fluid Mech.* **93**, 209–224.

GOLDSTEIN, M. E. 1997 Response of the pre-transitional laminar boundary layer to free stream turbulence. *Otto Laporte Lecture, Bull. Am. Phys. Soc.* **42**, 2150.

GOLDSTEIN, M. E. & LIEB, S. J. 1993 Three-dimensional boundary-layer instability and separation induced by small-amplitude streamwise vorticity in the upstream flow. *J. Fluid Mech.* **246**, 21–41.

GOLDSTEIN, M. E., LIEB, S. J. & COWLEY, S. J. 1992 Distortion of a flat-plate boundary layer by free-stream vorticity normal to the plate. *J. Fluid Mech.* **237**, 231–260.

HUNT, J. C. R. & CARRUTHERS, D. H. 1990 Rapid distortion theory and the 'problems' of turbulence. *J. Fluid Mech.* **212**, 497–532.

JAMESON, A. 1991 Time-dependent calculation using multigrid with application to unsteady flow past airfoils and wings. *AIAA Paper* 91-1596.

JAMESON, A., SCHMIDT, W., TURKEL, E. 1981 Numerical solutions of the Euler equations by finite volume methods using Runge–Kutta time-stepping schemes. *AIAA Paper* 81-1259.

KELLER, H. B. & CEBECI, T. 1972 Accurate numerical methods for boundary layer flows. *AIAA J.* **10**, 1193–1199.

KENDALL, J. M. 1991 Studies on laminar boundary-layer receptivity to freestream turbulence near a leading edge. In *Boundary Layer Stability and Transition to Turbulence* (ed. D. C. Reda, H. L. Reed & R Kabayashi). PP. 23–30. ASME.

KENNEDY, C. A. & CARPENTER, M. H. 1994 Several new numerical methods for compressible shear layer simulations. *Appl. Num. Maths* **14**, 397–433.

KINGMANN, B. G. B., BOIKO, A. V., WESTIN, K. J. A. KOZLOV, V. V. & ALFREDSSON, P. H. 1993 Experiments on the stability of Tollmien-Schlichting waves. *Eur. J. Mech.* B. *Fluids* **12**, 493–514

KUPFER, K., BERS, A. & RAM, A. K. 1987 The cusp map in the complex-frequency plane for absolute instabilities. *Phys. Fluids* **30**, 3075–3082.

LIGHTHILL, M. J. 1956 Drift. *J. Fluid Mech.* **1**, 31–33.

NAGARAJAN, S., LELE, S. K. & FERZIGER, J. H. 2007 Leading-edge effects in bypass transition. *J. Fluid Mech.* **572,** 471–504.

NAYFEH, A. H. 1973 *Perturbation Methods*. John Wiley.

SUSLOV, S. A. 2006 Numerical aspects of searching convective/absolute instability transition. *J. Comput. Phys.* **212**, 188–217.

TOOMRE, A. 1960 The viscous secondary flow ahead of an infinite cylinder in a uniform parallel shear flow. *J. Fluid Mech.* **7**, 145–155.

WATMUFF, J. 1997 Detrimental effects of almost immeasurably small free-stream nonuniformities generated by wind tunnel screens. *AIAA Paper* 97-0228.

WESTIN, K. J. A., BOIKO, A. V., KLINGMANN, B. G. B., KOZLOV, V. V. & ALFREDSSON, P. H. 1994 Experiments in a boundary layer subjected to free stream turbulence. Part 1. Boundary layer structure and receptivity. *J. Fluid Mech.* **281**, 193–218.

WU, X. 1992 The Nonlinear evolution of high-frequency resonant-triad waves in an oscillatory Stokes layer at high Reynolds number, *J. Fluid Mech.* **245**, 553–597.

WU, X. & CHOUDHARI, M. 2003 Linear and nonlinear instabilities of a Blasius boundary layer perturbed streamwise vortices. Part 2. Intermittent instability induced by long wavelength Klebanoff modes. *J. Fluid Mech.* **483**, 249–286.

WU, X. LEE, S. S. & COWLEY, S. J. 1993 On the weakly nonlinear three-dimensional instability of shear layers to pairs of oblique modes: the Stokes layer as a paradigm. *J. Fluid Mech.* **253**, 681–721.

WUNDROW, D. W. & GOLDSTEIN, M. E. 2001 Effect on a laminar boundary layer of small-amplitude streamwise vorticity in the upstream flow. *J. Fluid Mech.* **426**, 229–262.